
Excitation of the Forbidden Octupole Transition in $^{172}\text{Yb}^+$ Coulomb Crystals

Masterarbeit

an der Leibniz Universität Hannover

von

Chih-Han Yeh

geboren am 20. November 1993 in Taichung, Taiwan

Matrikelnr. 10008279

2019

Referent: PD. Dr. Tanja E. Mehlstäubler
Korreferent: Prof. Dr. Christian Ospelkaus

Hiermit erkläre ich, dass ich die vorliegende Arbeit selbstständig und ohne fremde Hilfe verfasst und keine anderen Hilfsmittel als angegeben verwendet habe. Die vorliegende Arbeit ist frei von Plagiaten. Alle Ausführungen, die wörtlich oder inhaltlich aus anderen Werken entnommen sind, habe ich als solche kenntlich gemacht. Diese Arbeit wurde in gleicher oder ähnlicher Form noch bei keinem anderen Prüfer als Prüfungsleistung eingereicht und ist auch noch nicht veröffentlicht.

Chih-Han Yeh

Abstract

Quantum field theory successfully unified the weak interaction, the strong interaction, and the electromagnetic field. However, the unification of quantum field theory and the gravitational field has so far been challenging. Therefore, attempts on the modification of the General Theory of Relativity have been made. Since the outcomes of the theory are derived from the basic principles, it is worthwhile to investigate the basis of gravitational physics. One of the basic assumptions is the Local Lorentz Invariance.

Within the framework of the Standard Model Extension, the breaking of Lorentz symmetry is inevitable. It suggests to measure a possible Lorentz violation signal in different particle sectors. In the electron sector, this signal is expected to be accessible at a small energy scale, as provided by atomic transitions in quantum optics experiments. Experimental tests on Lorentz symmetry in the electron sector have already been carried out with neutral Dy atoms, Ca^+ ions, and Yb^+ ions. The latter hosts the current record in the upper bound limit of the Lorentz violation parameter $\Delta C_0^{(2)}$ provided by the theory being 8.1×10^{-21} .

The main goal of our work is to test the validity of Lorentz symmetry and set a new upper bound via the approach of trapping multiple $^{172}\text{Yb}^+$ ions in a linear radio-frequency Paul trap. This thesis gives the theoretical background of the Lorentz violation in the electron sector and discusses four different schemes to measure the signal. The first three schemes are based on producing decoherence-free states via quantum correlation and the latter performs the experiment via dynamical decoupling. A laser with 12 mW of optical power at the ion has been set up for the interrogation of the octupole transition near 467 nm. It is used to excite the ions to the $^2F_{7/2}$ manifold which has a lifetime of ≈ 6 years. The alignment of the laser has been done via monitoring the induced AC-Stark shift of it on the quadrupole transition at 411 nm. With the selected laser beam parameters for the first attempt to interrogate this transition, a π -pulse time of ≈ 54 ms is to be expected.

With the sensitivity to a possible signal $\Delta C_0^{(2)}$ via dynamical decoupling being comparable with quantum correlation and not needing to worry about state decoherence during the state transfer which makes it easier to operate, we decided to follow the approach of implementing dynamical decoupling on the $^2F_{7/2}$ manifold. The measurement of $\Delta C_0^{(2)} = 8.1 \times 10^{-21}$ took an averaging time of 120 h. With the same averaging time, 10 ions, and 10 s of interrogation time, we would be able to reach a sensitivity

of $\Delta C_0^{(2)} = 4.7 \times 10^{-22}$ which would be a factor of 17 better than the current upper bound limit of $\Delta C_0^{(2)}$. With 2 ions and 1 s of interrogation time, we would be able to reach a sensitivity that is compatible to 8.1×10^{-21} within 24 h of averaging time.

Keywords: Lorentz violation, radio-frequency Paul trap, octupole transition, dynamical decoupling

Contents

1. Introduction	1
2. Discussion on the Lorentz violation theory and detection schemes	5
2.1. The theoretical background for the Lorentz violation in the electron sector	6
2.2. State transformation relations	9
2.3. Scheme 1: Preparing a product state which dephases into a mixed state	10
2.4. Scheme 2: Direct mapping of the ions onto the $^2F_{7/2}$ state via two-frequency bichromatic laser	14
2.5. Scheme 3: Using a Mølmer Sørensen gate to produce fully entangled state	17
2.6. Scheme 4: Using dynamical decoupling to produce a mixture of Zeeman substates	19
2.7. Sensitivity estimations and comparison of scheme 1-4	23
3. Experimental setup	27
3.1. The octupole laser for the $^{171}\text{Yb}^+$ single-ion optical clock	27
3.2. 934nm breadboard	28
3.2.1. Slave diode lasers	29
3.2.2. High frequency AOM	32
3.2.3. Sealed slave	32
3.3. 467nm SHG breadboard	37
4. Octupole transition of a single $^{172}\text{Yb}^+$ ion	41
4.1. Octupole selection rules	41
4.2. Experimental parameters	45
4.2.1. Beam waist and pulse time	45
4.2.2. Beam alignment procedure	46
4.2.3. Pulse sequence	51
5. Summary and outlook	53
Appendix A. Mathematica Code	61
A.1. Calculation of Rabi frequency and π -pulse time	61
A.2. Calculation of the AC-Stark shift and relative shift due to intensity fluctuation	65

1. Introduction

The theory of General Relativity is one of the most successful theories of the last century and is an important cornerstone of modern physics. However, the unification of the four forces (the weak interaction, the strong interaction, the electromagnetic field, the gravitational field) has not been successful. In order to unify them, there has been suggestions that modifications of gravitational physics are needed. It is worthwhile to investigate the basis of gravitational physics and one of the fundamental symmetries of the General Theory of Relativity is the Lorentz symmetry [1] (LS). It is one of the three pillars of the Einstein's Equivalence Principle (see Fig. 1.1) and suggests that the laws of physics stay the same for all observers that are moving with respect to one another within an inertial frame.

Well-known tests of this important cornerstone of modern physics are Michelson-Morley-type experiments verifying the isotropy of the speed of light [2–4]. For testing matters, Hughes-Drever-type experiments [5–10] test whether the kinetic energy of particles is independent of the direction of their velocity, i.e. whether their dispersion relations are isotropic. To provide more guidance for physics beyond the standard model, there have been theoretical suggestions that LS may not be exactly invariant at experimentally inaccessible energy scales. The possibilities of four-dimensional Lorentz violation (LV) has been investigated though not conclusively in various quantum gravity models such as string theory [11, 12], and loop quantum gravity [13].

LV may be possible in different systems, making it essential to verify with different particles at high precision. Tests have been conducted for photons [2, 14], protons [15], neutrons [10, 16], electrons [7, 17, 18], muons [19], and neutrinos [20, 21]. The summary of all limits before the year 2011 are given in Ref. [22]. While the natural energy scale for strong LV induced by quantum gravity is the Planck scale (at GeV level), the consequences of Lorentz violating physics may also lead to a very small but potentially observable low-energy (at eV level) LV signal. According to the Standard Model Extension [22–24] (SME), the measurement of the LV signal can be conducted in different sectors and one of them is the electron sector. Right now, the most sensitive LV tests in the electron sector are conducted with neutral Dy atoms [7], Ca^+ ions [18], and Yb^+ ions [25] with the latter hosting the current record of the upper bound limit of the LV parameter $\Delta C_0^{(2)}$ provided by the theory being 8.1×10^{-21} within 120 h

1. Introduction

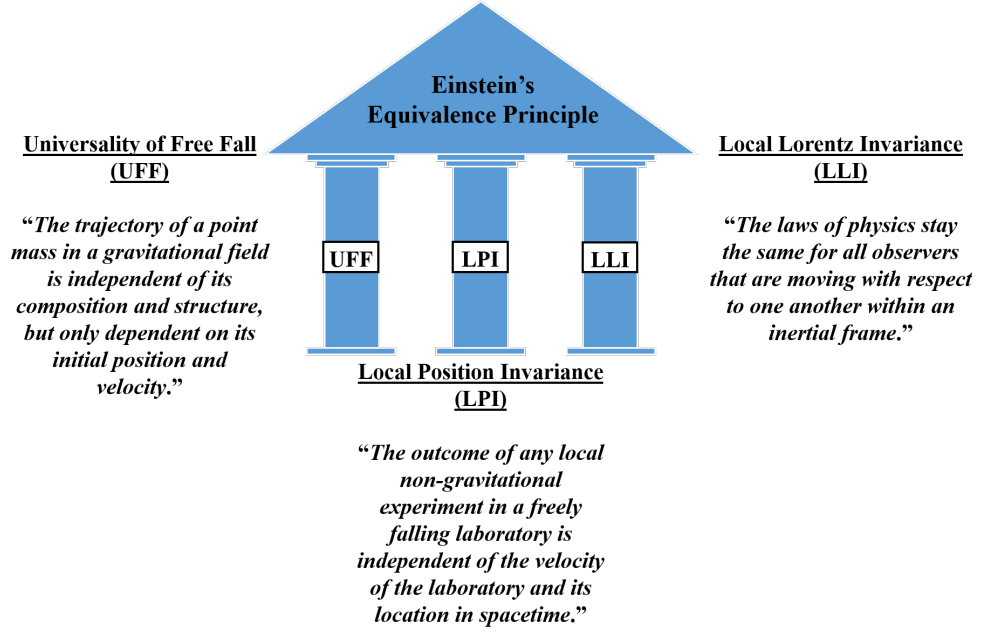


Figure 1.1.: The basic assumptions of the Einstein's equivalence principle.

of averaging time.

This thesis is organized as follows:

- In **chapter 2** the theoretical background for LV in the electron sector is discussed. Four schemes for the detection of a possible LV signal with $^{172}\text{Yb}^+$ are presented. Scheme 1 to 3 are based on quantum correlation which allows the states of the ions to become insensitive to external magnetic field fluctuation. Scheme 4 implements dynamical decoupling on the $^2F_{7/2}$ manifold such that the Zeeman substates are mixed and the states of the ions are insensitive to the magnetic field during the accumulation of a possible LV phase signal. To its end, the sensitivities of the schemes are calculated and compared with each other. This chapter concludes with the most favored method.
- In **chapter 3** the preparation for the 467 nm octupole laser light is presented. The setup consists of two main breadboards. The first part is the 934 nm laser breadboard which has two purposes: to enhance the fractional amount of the optical power that is shared with an optical clock experiment that uses $^{171}\text{Yb}^+$, and to bridge the frequency gap between the two Yb^+ isotopes. The second part is the 467 nm laser breadboard which is used to obtain the 467 nm laser light for

the interrogation of the octupole transition.

- In **chapter 4** the octupole selection rules and the experimental parameters for the interrogation of the octupole transition are discussed. The pulse sequence for the interrogation is presented.
- In **chapter 5** the conclusion with a proposal for implementing dynamical decoupling on the $^2F_{7/2}$ manifold of $^{172}\text{Yb}^+$ for the test of LV is made. Then the outlook on the next steps to be taken in the experiment is given.

2. Discussion on the Lorentz violation theory and detection schemes

In this chapter, the theoretical background for the LV in the electron sector is first presented. The state transformation relations and four different schemes for detecting the LV signal are discussed.

The state we use to perform a test of LV is the F manifold in the even isotope $^{172}\text{Yb}^+$. During the accumulation of this possible LV signal, the state needs to be protected from the magnetic field noise. In order to suppress the noise in the first order, one of the ways is to prepare the ions in an entangled state with the average of the linear Zeeman shift being zero via quantum correlation and thus insensitive to the magnetic field noise. However, the scaling of the numbers of ions with quantum correlation is limited and hard to obtain. A promising technique to implement dynamical decoupling in the $^2F_{7/2}$ manifold. With this method, less optical pulses are needed, no AC-Stark shift will be present due to radio-frequency (RF) operations, and measurements can be done with multiple ions.

The π -pulse time for this highly forbidden transition is at the level of tens of milliseconds. During this time, the magnetic field noise may couple into the state and cause dephasing because this isotope does not have a magnetic field noise insensitive transition. Therefore, the magnetic field needs to be actively stabilized.

After the discussion of the four schemes, their sensitivities to a possible LV signal are calculated and compared.

The schemes will be discussed in the following order:

- **Scheme 1** [17]: preparing a superposition state with two ions that dephases into a mixed state which contains the desired decoherence-free entangled state with 50% probability [17]. Then the desired state is mapped onto the $^2F_{7/2}$ state for a possible LV signal accumulation.
- **Scheme 2**: implementing a two-frequency bichromatic laser to prepare a superposition state similar to scheme 1 that dephases into a mixed state. The desired

2. Discussion on the Lorentz violation theory and detection schemes

state for a possible LV signal detection is populated with 50% probability.

- **Scheme 3** [18]: implementing a Mølmer Sørensen gate [26–28] to entangle the two ions to obtain the desired state with 100% probability [18] for a possible LV signal detection.
- **Scheme 4**: implementing dynamical decoupling on the $^2F_{7/2}$ manifold. It is a robust method which can easily scaled up to higher ion numbers. It also reduces the number of required optical pulses which suppresses the effect of laser induced AC-Stark shift. A composite RF-pulse is implemented for the accumulation of a possible LV signal.

2.1. The theoretical background for the Lorentz violation in the electron sector

The LV is typically studied in the framework of the SME. It can be used to describe the low-energy limit that predicts LV, and also includes the standard model as a limiting case. It provides a universal platform to compare all kinds of LV measurements [24].

In the electron sector, a hypothetical LV is quantified in the SME by adding a symmetry-breaking $c'_{\mu\nu}$ tensor to the kinetic term in the standard model Lagrangian. In the context of clock experiments, the LV in bound electronic states leads to a small shift of the energy level described by a Hamiltonian [7, 29]

$$\delta\hat{\mathcal{H}} = - \left(C_0^{(0)} - \frac{2U}{3c_0^2} c'_{00} \right) \frac{\mathbf{p}^2}{2} - C_0^{(2)} \frac{\hat{T}_0^{(2)}}{6m_e}, \quad (2.1)$$

where \mathbf{p} is the momentum of a bound electron, U is the Newtonian potential and c_0 is the speed of light. The parameter $C_0^{(0)}$, $C_0^{(2)} = c_{xx} + c_{yy} - 2c_{zz}$, and c'_{00} are elements of the $c'_{\mu\nu}$ tensor that characterizes the LV. The $\hat{T}_0^{(2)}$ is the corresponding component of the quadruple moment operator of the electronic momentum distribution. The non-relativistic form of the $\hat{T}_0^{(2)}$ operator is $\hat{T}_0^{(2)} = \mathbf{p}^2 - 3p_z^2$, where p_z is the component of the momentum along the quantization axis, and the relativistic form is $\hat{T}_0^{(2)} = c\gamma_0(\boldsymbol{\gamma}\mathbf{p} - 3\gamma^z p_z)$, where γ_0 , γ^z and $\boldsymbol{\gamma}$ are the Dirac matrices. The first part of Equ. 2.1 is a constant for the certain type of elements chosen, and the second part is the part we are interested in. The parameter $C_0^{(2)}$ will vary if the LS is violated. If the Lorentz symmetry is invariant, the tensor becomes zero.

There are two different approaches to measure the cause of a possible LV to the energy levels:

2.1. The theoretical background for the Lorentz violation in the electron sector

1. Measure the absolute frequencies of an optical transition with differently oriented quantization axis, then compare the frequency difference between them.
2. Using two Zeeman substates that have differently oriented wave packets and measure the energy level difference between them.

The first approach was implemented in the experiment of Ref. [25] where two $^{171}\text{Yb}^+$ single-ion optical clocks operating on the $^2S_{1/2} \leftrightarrow ^2F_{7/2}$ electric octupole transition with quantization axes aligned along nonparallel directions were used and the frequencies of them were compared continuously. According to SME, the signal of a possible LV would manifest itself as the quantization axis rotate. In the Earth frame, it would be a sidereal modulation of the frequency offset. From the absence of such modulation of the frequency difference at the 10^{-19} level, the stringent limits on LV parameters for electrons are pushed to the range of 10^{-21} .

The approach we follow is the second one. With the second approach we are more sensitive to a possible LV signal as will be discussed in Section 2.7. The calculation of the energy shift due to possible LV can be reduced to the calculation of the expectation value of the Hamiltonian in Equ. 2.1. The matrix element of the expectation value $\langle J, m_j | \hat{T}_0^{(2)} | J, m_j \rangle$ is expressed through the reduced matrix element of the $\hat{T}_0^{(2)}$ operator using the Wigner-Eckart theorem, becoming [7, 29]

$$\langle J, m_j | \hat{T}_0^{(2)} | J, m_j \rangle = (-1)^{J-m_j} \begin{pmatrix} J & 2 & J \\ -m_j & 0 & m_j \end{pmatrix} \langle J || \hat{T}^{(2)} || J \rangle, \quad (2.2)$$

where $\langle J || \hat{T}^{(2)} || J \rangle$ is the reduced matrix element. By using the algebraic expression for the $3j$ -symbol, we arrive at

$$\langle J, m_j | \hat{T}_0^{(2)} | J, m_j \rangle = \frac{-J(J+1) + 3m_j^2}{\sqrt{(2J+3)(J+1)(2J+1)J(2J-1)}} \langle J || \hat{T}^{(2)} || J \rangle. \quad (2.3)$$

where J is the quantum numbers of the total angular momentum and m_j is the projection onto the quantization axis. From the equation we see that the tensor of the Lorentz violating signal is proportional to m_j^2 . Therefore, the idea to obtain a possible LV signal is to monitor the energy difference between different m_j substates as the quantization axis rotates, and thus placing a bound to $C_0^{(2)}$. As depicted in Fig. 2.1, a magnetic bias field \vec{B} is applied vertically in the laboratory frame to define the quantization axis of the experiment. As the Earth rotates with an angular frequency of $\omega_E = 2\pi/(23.93 \text{ h})$, the orientation of the quantization axis and that of the electron wave packet changes with respect to the Sun's rest frame. The signal of a possible LV

2. Discussion on the Lorentz violation theory and detection schemes

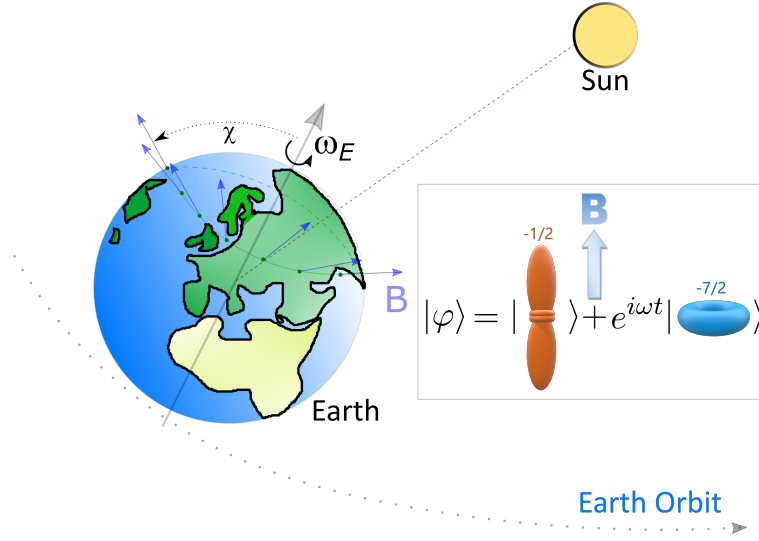


Figure 2.1.: Testing LV via the orthogonally orientated states. The Earth rotates with angular frequency ω_E about its polar axis while orbiting the Sun. The angle between the magnetic field \mathbf{B} applied for setting the quantization axis and the Earth's polar axis is defined as the colatitude of the experiment being χ .

will accumulate in the phase difference between $|F, -1/2\rangle$ and $|F, -7/2\rangle$ and present as $e^{i\omega t}$. The angle χ is the colatitude of the experiment.

From Eq. 2.3, the difference in the energy levels for a single ion caused by a possible LV acting on Yb^+ ions can be calculated as [30]

$$\frac{\Delta E}{h} = 5.11 \times 10^{15} \text{ Hz} \cdot (m_{J_2}^2 - m_{J_1}^2) \cdot C_0^{(2)}, \quad (2.4)$$

where m_{J_1} and m_{J_2} are the two Zeeman substates to be interrogated. If we interrogate the states $|F, \pm 1/2\rangle$ and $|F, \pm 7/2\rangle$, the energy difference is

$$\begin{aligned} \frac{\Delta E}{h} &= 5.11 \times 10^{15} \text{ Hz} \cdot \left[\left(\frac{7}{2} \right)^2 - \left(\frac{1}{2} \right)^2 \right] \cdot C_0^{(2)} \\ &= 6.14 \times 10^{16} \text{ Hz} \cdot C_0^{(2)}, \end{aligned} \quad (2.5)$$

In order to monitor the modulation of the energy level caused by LV, the population of the excited state is being monitored and fitted to a model being [18]

$$\nu = \frac{\Delta E}{h} = A \cdot \sin(\omega_E T + \varphi_A) + B \cdot \cos(2\omega_E T + \varphi_B), \quad (2.6)$$

where $\omega_E = 2\pi/(23.93 \text{ h})$ is the sidereal angular frequency of the Earth's rotation, T is the total integration time. The A , B , C , and D coefficients depend on the $c'_{\mu\nu}$ tensor. If a LV signal appears, then the local observable would oscillate at a half-day or a day period and could be seen when fitted to the model in Eq. 2.6.

During the accumulation of the signal, we need to suppress the first order fluctuation, specifically the magnetic field noise. Therefore, the state needs to be entangled such that the average Zeeman shift becomes zero, and thus the fluctuation caused by the magnetic field noise. For scheme 1 to 3, the main ideas are similar. Two ions are prepared via quantum correlation methods to produce the target state being $|\varphi\rangle = |F, -1/2\rangle|F, +1/2\rangle + |F, -7/2\rangle|F, +7/2\rangle$. With this state, the ions are most sensitive to a possible LV signal as is calculated in Equ. 2.5. In addition, the state is insensitive to magnetic field fluctuations in the first order. However, during the state preparation, laser induced AC-Stark shift will be present and the magnetic field noise may cause the state to dephase. The advantage for scheme 4 is that it reduces the number of optical pulses and features a suppressed sensitivity to the linear Zeeman effect.

2.2. State transformation relations

In the discussions of a possible LV detection schemes, the Rabi model of atom-light interaction is defined as [31] (assuming that the laser is on resonance with the transition frequency):

1. If the state is initially in the ground state

$$|g\rangle \rightarrow \cos\left(\frac{\theta}{2}\right)|g\rangle - ie^{-i\phi_T} \sin\left(\frac{\theta}{2}\right)|e\rangle; \quad (2.7)$$

2. If the state is initially in the excited state

$$|e\rangle \rightarrow -ie^{i\phi_T} \sin\left(\frac{\theta}{2}\right)|g\rangle + \cos\left(\frac{\theta}{2}\right)|e\rangle, \quad (2.8)$$

where $|g\rangle$ is the ground state, $|e\rangle$ is the excited state and θ is the pulse area. ϕ_T is the phase induced by the laser, which included the phase of the laser light path and the phase caused by the laser induced AC-Stark shift.

The linear Zeeman effect is also important since $^{172}\text{Yb}^+$ doesn't have hyperfine structure with $m_F = 0$ substate. The phase caused by the effect is given by

$$\phi_B = \frac{E}{\hbar}t = \frac{g_J\mu_B m_j |\mathbf{B}|}{\hbar}t, \quad (2.9)$$

2. Discussion on the Lorentz violation theory and detection schemes

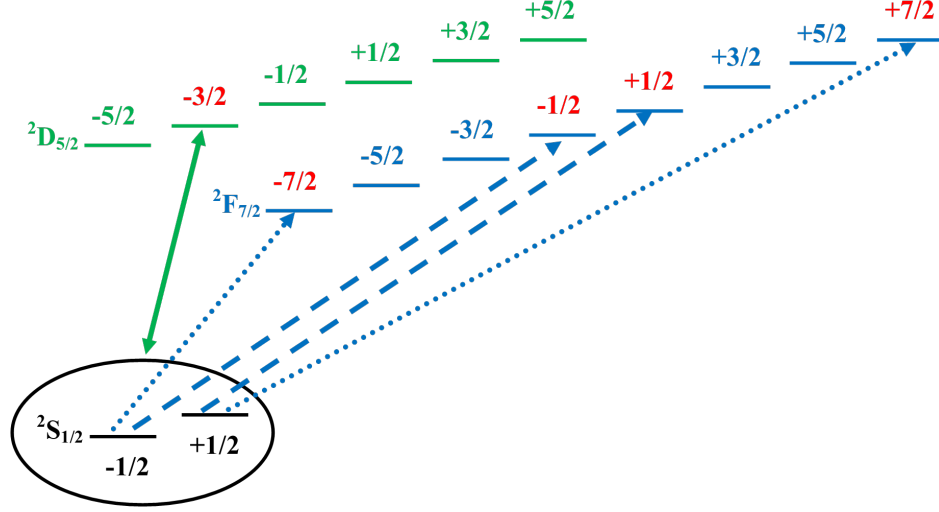


Figure 2.2.: Relevant energy levels for preparing a product state in the ${}^2F_{7/2}$ manifold. The solid, green, arrowed line is the mixed state preparation sequence such that the state of the two ions becomes $(|S, +1/2\rangle_1 |S, -1/2\rangle_2 + |S, -1/2\rangle_1 |S, +1/2\rangle_2)/\sqrt{2}$. The dotted lines correspond to the first simultaneous π -pulse that maps the first part of the state $|S, +1/2\rangle_1 |S, -1/2\rangle_2$ to $|F, +7/2\rangle_1 |F, -7/2\rangle_2$, and the dashed lines for the second simultaneous π -pulse that maps the second part $|S, -1/2\rangle_1 |S, +1/2\rangle_2$ to $|F, -1/2\rangle_1 |F, +1/2\rangle_2$ so that the final state becomes $(|F, +7/2\rangle_1 |F, -7/2\rangle_2 + |F, -1/2\rangle_1 |F, +1/2\rangle_2)/\sqrt{2}$ for a possible LV phase signal accumulation.

where m_j is the magnetic quantum number, μ_B is the Bohr magneton, g_J is the Landé factor for a certain state with total spin J , and \mathbf{B} is the magnetic field at the position of the ions.

2.3. Scheme 1: Preparing a product state which dephases into a mixed state

In this scheme, the intensities of the lasers that interrogate the two ions are first assumed to be identical. A product state is prepared and it dephases into a mixed state that consists of a decoherence-free entangled state with 50% probability [32].

To probe a possible LV, we simply monitor the energy difference between the two components of the target state $|\psi_B\rangle \rightarrow |F, +7/2\rangle_1 |F, -7/2\rangle_2 + |F, -1/2\rangle_1 |F, +1/2\rangle_2$ using the parity oscillation. The oscillation frequency from the parity signal is extracted by fitting the whole parity oscillation curve to the model presented in Eq. 2.6. However, this energy difference also depends on the magnetic field amplitude (causing

2.3. Scheme 1: Preparing a product state which dephases into a mixed state

the quadratic Zeeman effect), the magnetic field gradient, and the electric field gradient (causing the electric quadrupole shift) created by the trap.

To characterize the quadratic Zeeman effect, one can calculate it via [33, 34]

$$\frac{\Delta E_{\text{Zeeman}}^{(2)}}{\hbar} = 2\pi \times -2.12 \frac{\text{mHz}}{(\mu\text{T})^2} \cdot B \cdot \Delta B, \quad (2.10)$$

where B and ΔB are the average value of the magnetic field and its uncertainty, respectively.

To suppress the effect of the magnetic field gradient, we can measure the oscillation frequency from the parity signal of the state $|\psi_B^+\rangle = |F, +7/2\rangle_1 |F, -7/2\rangle_2 + |F, -1/2\rangle_2 |F, +1/2\rangle_1$ and $|\psi_B^-\rangle = |F, -7/2\rangle_1 |F, +7/2\rangle_2 + |F, +1/2\rangle_2 |F, -1/2\rangle_1$ to be f^+ and f^- , respectively. The contribution from the magnetic field gradient for these two states has an opposite sign. Therefore, the averaged frequency $f^0 = (f^+ + f^-)/2$ contains the possible LV signal, and the effect of the magnetic field gradient is suppressed.

To characterize the shift induced by the electric quadrupole effect, we can measure the frequency f^0 as a function of the electric field gradient in the trap by changing the axial secular frequency of the trap.

The two ions are optically pumped and prepared in the initial ground state of $|S, -1/2\rangle_1 |S, -1/2\rangle_2$, where the subscripts denote the respective ion. A $\pi/2$ -pulse with laser phase ϕ_{L1} (transforms $|S, -1/2\rangle \leftrightarrow |D, -3/2\rangle$) and a π -pulse with laser phase ϕ_{L2} (transforms $|D, -3/2\rangle \leftrightarrow |S, +1/2\rangle$) on both ions is applied in sequence to have

$$\begin{aligned} \bullet |A\rangle = \frac{1}{2} & \left[e^{i\phi_{(-1/2)}} e^{i\phi_{(-1/2)}} |S, -1/2\rangle_1 |S, -1/2\rangle_2 \right. \\ & + e^{2i(\phi_{L2} + \phi_{AC_{L2}} - \phi_{L1} - \phi_{AC_{L1}})} e^{i\phi_{(+1/2)}} e^{i\phi_{(+1/2)}} |S, +1/2\rangle_1 |S, +1/2\rangle_2 \\ & - e^{i(\phi_{L2} + \phi_{AC_{L2}} - \phi_{L1} - \phi_{AC_{L1}})} e^{i\phi_{(+1/2)}} e^{i\phi_{(-1/2)}} |S, +1/2\rangle_1 |S, -1/2\rangle_2 \\ & \left. - e^{i(\phi_{L2} + \phi_{AC_{L2}} - \phi_{L1} - \phi_{AC_{L1}})} e^{i\phi_{(-1/2)}} e^{i\phi_{(+1/2)}} |S, -1/2\rangle_1 |S, +1/2\rangle_2 \right], \end{aligned} \quad (2.11)$$

where $\phi_{AC_{L1}}$ and $\phi_{AC_{L2}}$ are the phases of the laser induced AC-Stark shifts. $\phi_{(-1/2)} = g_{1/2}\mu_B(-1/2)|\mathbf{B}|t/\hbar$ and $\phi_{(+1/2)} = g_{1/2}\mu_B(+1/2)|\mathbf{B}|t/\hbar$ are the phases caused by the linear Zeeman effect.

2. Discussion on the Lorentz violation theory and detection schemes

After the production of state $|A\rangle$, some waiting time can be applied. The average phase induced by the linear Zeeman effect for the states $|S, -1/2\rangle_1|S, -1/2\rangle_2$ and $|S, +1/2\rangle_1|S, +1/2\rangle_2$ does not equal to zero, meaning that they are not protected from magnetic field and will dephase, leaving only the state $|S, +1/2\rangle_1|S, -1/2\rangle_2$ and $|S, -1/2\rangle_1|S, +1/2\rangle_2$ that are protected from the magnetic field due to an average phase of zero. $|A\rangle$ becomes

$$\bullet |A\rangle \rightarrow -\frac{1}{2}e^{i(\phi_{L2}+\phi_{AC_{L2}}-\phi_{L1}-\phi_{AC_{L1}})}(|S, +1/2\rangle_1|S, -1/2\rangle_2 + |S, -1/2\rangle_1|S, +1/2\rangle_2). \quad (2.12)$$

Since $e^{i(\phi_{L2}+\phi_{AC_{L2}}-\phi_{L1}-\phi_{AC_{L1}})}$ is outside of the bracket of Eq. 2.12, i.e. the phase will not show an effect if the population of the state is to be detected, so we simplify it such that $\phi_{L2} + \phi_{AC_{L2}} - \phi_{L1} - \phi_{AC_{L1}} = 0 \Rightarrow e^{i(\phi_{L2}+\phi_{AC_{L2}}-\phi_{L1}-\phi_{AC_{L1}})} = 1$. $|A\rangle$ is simplified as

$$\bullet |A\rangle \rightarrow -\frac{1}{2}(|S, +1/2\rangle_1|S, -1/2\rangle_2 + |S, -1/2\rangle_1|S, +1/2\rangle_2). \quad (2.13)$$

With the mixed state $|A\rangle$, four different π -pulses with laser phase $\phi_1, \phi_2, \phi_3, \phi_4$ correspondingly are applied with single ion addressing, as can be seen in Fig. 2.2, transforming the state into $|B\rangle$. Two pairs of pulses are applied, where in each pair each laser addresses only one ion. The first pair of π -pulses maps the population in $|S, +1/2\rangle$ to $|F, +7/2\rangle$ and the population in $|S, -1/2\rangle$ to $|F, -7/2\rangle$. The second pair of pulses maps the remaining population of each ion from $|S, -1/2\rangle$ to $|F, -1/2\rangle$ and $|S, +1/2\rangle$ to $|F, +1/2\rangle$. Thus the state $|B\rangle$ reads:

$$\begin{aligned} \bullet |B\rangle &= \frac{1}{\sqrt{2}}|\psi_B\rangle \\ &= \frac{1}{2}\left[e^{-i(\phi_1+\phi_{AC_1}+\phi_2+\phi_{AC_2})}|F, +7/2\rangle_1|F, -7/2\rangle_2 \right. \\ &\quad \left. + e^{-i(\phi_3+\phi_{AC_3}+\phi_4+\phi_{AC_4})}|F, -1/2\rangle_1|F, +1/2\rangle_2\right], \end{aligned} \quad (2.14)$$

where $\phi_{AC_1}, \phi_{AC_2}, \phi_{AC_3}$, and ϕ_{AC_4} are the AC-Stark shifts induced by the 4 different laser pulses. $|\psi_B\rangle$ is the desired state. Next, one waits the time T to accumulate a potential phase shift due to LV. It induces a relative phase shift $e^{i\delta T} = e^{i\psi}$ to the desired state $|\psi_B\rangle$, such that

$$\begin{aligned} \bullet |\psi_B\rangle &= \frac{1}{\sqrt{2}}\left[e^{i\psi} \cdot e^{-i(\phi_1+\phi_{AC_1}+\phi_2+\phi_{AC_2})}|F, +7/2\rangle_1|F, -7/2\rangle_2 \right. \\ &\quad \left. + e^{-i(\phi_3+\phi_{AC_3}+\phi_4+\phi_{AC_4})}|F, -1/2\rangle_1|F, +1/2\rangle_2\right]. \end{aligned} \quad (2.15)$$

2.3. Scheme 1: Preparing a product state which dephases into a mixed state

To extract the possible LV signal, the state is manipulated by operating the pulses the other way around, i.e. four π -pulses with laser phase $\phi'_1, \phi'_2, \phi'_3, \phi'_4$, respectively. Two pairs of pulses are applied, where in each pair each laser addresses only one ion. The first pair of π -pulses maps the population in $|F, +7/2\rangle$ back to $|S, +1/2\rangle$ and the population in $|F, -7/2\rangle$ to $|S, -1/2\rangle$. The second pair of pulses maps $|F, -1/2\rangle$ to $|S, -1/2\rangle$ and $|F, +1/2\rangle$ to $|S, +1/2\rangle$,

$$\bullet |\psi'_B\rangle = -\frac{1}{\sqrt{2}} \left[e^{i\psi} \cdot e^{i(\varphi_1 + \varphi_{AC1} + \varphi_2 + \varphi_{AC2})} |S, +1/2\rangle_1 |S, -1/2\rangle_2 \right. \\ \left. + e^{i(\varphi_3 + \varphi_{AC3} + \varphi_4 + \varphi_{AC4})} |S, -1/2\rangle_1 |S, +1/2\rangle_2 \right], \quad (2.16)$$

where $\varphi_k = \phi'_k - \phi_k$ and $\varphi_{AC_k} = \phi'_{AC_k} - \phi_{AC_k}$, ($k = 1, \dots, 4$). Next, a π -pulse is applied on both ions with laser phase ϕ'_{L2} (transforms $|S, +1/2\rangle \leftrightarrow |D, -3/2\rangle$),

$$\bullet |\psi'_B\rangle \rightarrow \frac{i}{\sqrt{2}} e^{-i(\phi'_{L2} + \phi'_{ACL2})} \left[e^{i\psi} \cdot e^{i(\varphi_1 + \varphi_{AC1} + \varphi_2 + \varphi_{AC2})} |D, -3/2\rangle_1 |S, -1/2\rangle_2 \right. \\ \left. + e^{i(\varphi_3 + \varphi_{AC3} + \varphi_4 + \varphi_{AC4})} |S, -1/2\rangle_1 |D, -3/2\rangle_2 \right]. \quad (2.17)$$

By setting $e^{-i(\phi'_{L2} + \phi'_{ACL2})} = 1$, and applying a $\pi/2$ -pulse of laser phase ϕ'_{L1} (transforms $|D, -3/2\rangle \leftrightarrow |S, -1/2\rangle$), the state becomes

$$\bullet 2\sqrt{2}|\psi'_B\rangle \rightarrow e^{i(\phi'_{L1} + \phi'_{ACL1})} \left[e^{i\psi} \cdot e^{i(\varphi_1 + \varphi_{AC1} + \varphi_2 + \varphi_{AC2})} + e^{i(\varphi_3 + \varphi_{AC3} + \varphi_4 + \varphi_{AC4})} \right] \\ \cdot |S, -1/2\rangle_1 |S, -1/2\rangle_2 \\ + e^{-i(\phi'_{L1} + \phi'_{ACL1})} \left[e^{i\psi} \cdot e^{i(\varphi_1 + \varphi_{AC1} + \varphi_2 + \varphi_{AC2})} + e^{i(\varphi_3 + \varphi_{AC3} + \varphi_4 + \varphi_{AC4})} \right] \\ \cdot |D, -3/2\rangle_1 |D, -3/2\rangle_2 \\ + i \left[e^{i\psi} \cdot e^{i(\varphi_1 + \varphi_{AC1} + \varphi_2 + \varphi_{AC2})} - e^{i(\varphi_3 + \varphi_{AC3} + \varphi_4 + \varphi_{AC4})} \right] |D, -3/2\rangle_1 |S, -1/2\rangle_2 \\ + i \left[e^{i(\varphi_3 + \varphi_{AC3} + \varphi_4 + \varphi_{AC4})} - e^{i\psi} \cdot e^{i(\varphi_1 + \varphi_{AC1} + \varphi_2 + \varphi_{AC2})} \right] |S, -1/2\rangle_1 |D, -3/2\rangle_2. \quad (2.18)$$

For simple reading, we define $|S, -1/2\rangle_1 |S, -1/2\rangle_2 \equiv |SS\rangle$, $|D, -3/2\rangle_1 |D, -3/2\rangle_2 \equiv |DD\rangle$, $|D, -3/2\rangle_1 |S, -1/2\rangle_2 \equiv |DS\rangle$, and $|S, -1/2\rangle_1 |D, -3/2\rangle_2 \equiv |SD\rangle$. The diagonal

2. Discussion on the Lorentz violation theory and detection schemes

term of the density matrix of the state $|B\rangle = |\psi'_B\rangle/\sqrt{2}$ is

$$\begin{aligned}
 \bullet |B\rangle\langle B| &= \frac{1}{2 \times 8} \\
 &\times \left\{ [2 + 2 \cos(\psi + \Delta)] |SS\rangle\langle SS| + [2 + 2 \cos(\psi + \Delta)] |DD\rangle\langle DD| \right. \\
 &\quad \left. + [2 - 2 \cos(\psi + \Delta)] |DS\rangle\langle DS| + [2 - 2 \cos(\psi + \Delta)] |SD\rangle\langle SD| \right\} \\
 &= P_{SS} \cdot |SS\rangle\langle SS| + P_{DD} \cdot |DD\rangle\langle DD| + P_{DS} \cdot |DS\rangle\langle DS| + P_{SD} \cdot |SD\rangle\langle SD|,
 \end{aligned} \tag{2.19}$$

where $\Delta := \varphi_1 + \varphi_{AC_1} + \varphi_2 + \varphi_{AC_2} - \varphi_3 - \varphi_{AC_3} - \varphi_4 - \varphi_{AC_4}$. P_{SS} , P_{DD} , P_{DS} , and P_{SD} are the probabilities of finding the ions in the corresponding states. Hence, the parity oscillation signal given by $P = P_{SS} + P_{DD} - P_{DS} - P_{SD}$ is

$$P = P_{SS} + P_{DD} - P_{DS} - P_{SD} = \frac{1}{2} \cos(\psi + \Delta), \tag{2.20}$$

where $1/2$ comes from the fact that only half of the mixed state was protected from the magnetic field.

In actual experiments, the intensity of the laser on each ion is not the same, this causes a relative phase between the two addressing lasers. Eq. 2.13 becomes

$$- \frac{1}{2} (e^{i\phi_{XY}} |S, +1/2\rangle_1 |S, -1/2\rangle_2 + |S, -1/2\rangle_1 |S, +1/2\rangle_2), \tag{2.21}$$

where $e^{i\phi_{XY}}$ is the relative phase between the two ions while preparing the mixed state. Since this relative phase term acts the same way as the LV phase signal, the parity oscillation signal becomes

$$P = P_{SS} + P_{DD} - P_{DS} - P_{SD} = \frac{1}{2} \cos(\psi + \Delta + \phi_{XY}). \tag{2.22}$$

2.4. Scheme 2: Direct mapping of the ions onto the $^2F_{7/2}$ state via two-frequency bichromatic laser

Different from scheme 1 [17], the advantage of using a two-frequency bichromatic laser is that it can directly map the initial state to the $^2F_{7/2}$ manifold rather than first preparing the state to the magnetic field protected $|S, +1/2\rangle_1 |S, -1/2\rangle_2 + |S, -1/2\rangle_1 |S, +1/2\rangle_2$ with subsequent mapping to the $^2F_{7/2}$ substates. This scheme would be of advantage

2.4. Scheme 2: Direct mapping of the ions onto the $^2F_{7/2}$ state via two-frequency bichromatic laser

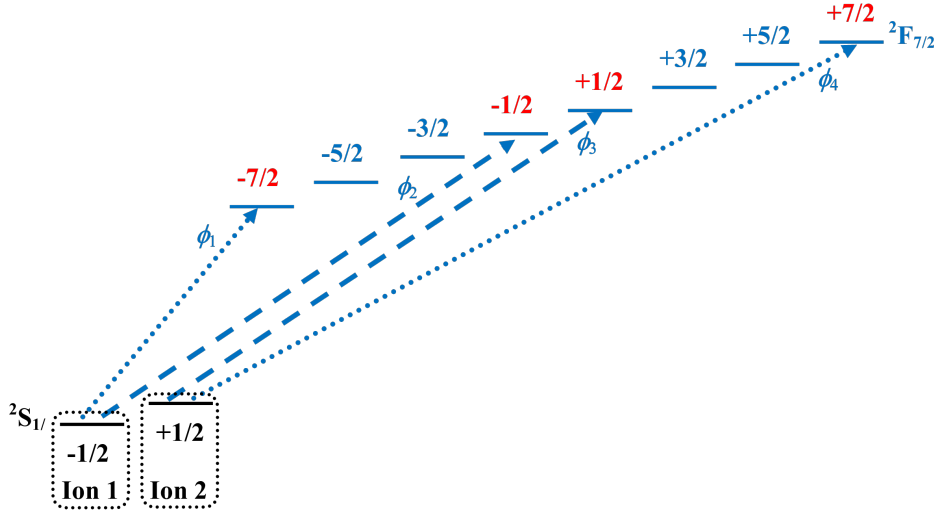


Figure 2.3.: Relevant energy levels for preparing the mixed state using a two-frequency bichromatic laser. The initial state is prepared into $|S, -1/2\rangle_1 |S, +1/2\rangle_2$ and with the octupole laser, the mixed state is created directly on the $^2F_{7/2}$ manifold. ϕ_1 to ϕ_4 are defined as $\pi/2$ -pulse laser phases.

if the magnetic field is so stable that the state during the pulse time does not dephase. The total optical pulse interrogation time of each measurement cycle would be decreased by a π -pulse time: the total interrogation time with the octupole laser would be the sum of two π -pulses and two $\pi/2$ -pulses while scheme 1 requires a total interrogation time of four π -pulses.

As shown in Fig. 2.3, the initial state needs to be prepared as $|S, -1/2\rangle_1 |S, +1/2\rangle_2$ via addressing each ion individually with different circular polarized light. $\pi/2$ - and π -pulses are applied to obtain the desired state for detection. The $\pi/2$ -pulse laser phases are defined as

$$\begin{aligned}\phi_1 &:= |S, -1/2\rangle \leftrightarrow |F, -1/2\rangle; \\ \phi_2 &:= |S, -1/2\rangle \leftrightarrow |F, -7/2\rangle; \\ \phi_3 &:= |S, +1/2\rangle \leftrightarrow |F, +1/2\rangle; \\ \phi_4 &:= |S, +1/2\rangle \leftrightarrow |F, +7/2\rangle.\end{aligned}\tag{2.23}$$

First, a pair of $\pi/2$ -pulses is applied, where the laser with phase ϕ_1 acts on ion 1 and ϕ_4 acts on ion 2. Next, a pair of π -pulses is applied with ϕ_2 on ion 1 and ϕ_3 on ion 2. The states proportional to $|F, -7/2\rangle_1 |F, +1/2\rangle_2$ and $|F, -1/2\rangle_1 |F, +7/2\rangle_2$ dephase since they are not protected from the magnetic field, leaving only the states $|F, -1/2\rangle_1 |F, +1/2\rangle_2$ and $|F, -7/2\rangle_1 |F, +7/2\rangle_2$. With some waiting time T , a possible

2. Discussion on the Lorentz violation theory and detection schemes

LV phase signal is accumulated

$$\begin{aligned}
 \bullet |B\rangle &= \frac{1}{\sqrt{2}}|\psi_B\rangle \\
 &= \frac{1}{2} \left[e^{i\psi} \cdot e^{-i(2\phi_2+\phi_4+2\phi_{AC_2}+\phi_{AC_4})} |F, -7/2\rangle_1 |F, +7/2\rangle_2 \right. \\
 &\quad \left. + e^{-i(\phi_1+2\phi_3+\phi_{AC_1}+2\phi_{AC_3})} |F, -1/2\rangle_1 |F, +1/2\rangle_2 \right].
 \end{aligned} \tag{2.24}$$

And with the $\pi/2$ - and π -pulses operated the other way around

$$\begin{aligned}
 \bullet |\psi'_B\rangle &= \frac{i}{2\sqrt{2}} \left\{ i \left[e^{i\psi} \cdot e^{i(2\varphi_2+2\varphi_{AC_2}+\varphi_4+\varphi_{AC_4})} + e^{i(\varphi_1+\varphi_{AC_1}+2\varphi_3+2\varphi_{AC_3})} \right] \right. \\
 &\quad \cdot |S, -1/2\rangle_1 |S, +1/2\rangle_2 \\
 &\quad + \left[e^{i\psi} \cdot e^{i(2\varphi_2+2\varphi_{AC_2}+\varphi_4+\varphi_{AC_4})} e^{-i(\phi'_1+\phi'_{AC_1})} - e^{i(2\varphi_3+2\varphi_{AC_3})} e^{-i(\phi_1+\phi_{AC_1})} \right] \\
 &\quad \cdot |F, -1/2\rangle_1 |S, +1/2\rangle_2 \\
 &\quad + \left[e^{i(\varphi_1+\varphi_{AC_1}+2\varphi_3+2\varphi_{AC_3})} e^{-i(\phi'_4+\phi'_{AC_4})} - e^{i\psi} \cdot e^{i(2\varphi_2+2\varphi_{AC_2})} e^{-i(\phi_4+\phi_{AC_4})} \right] \\
 &\quad \cdot |S, -1/2\rangle_1 |F, +7/2\rangle_2 \\
 &\quad + i \left[e^{i\psi} \cdot e^{i(2\varphi_2+2\varphi_{AC_2})} e^{-i(\phi'_1+\phi'_{AC_1}+\phi_4+\phi_{AC_4})} + e^{i(2\varphi_3+2\varphi_{AC_3})} e^{-i(\phi_1+\phi_{AC_1}+\phi'_4+\phi'_{AC_4})} \right] \\
 &\quad \cdot |F, -1/2\rangle_1 |F, +7/2\rangle_2 \Big\},
 \end{aligned} \tag{2.25}$$

where $\varphi_k = \phi'_k - \phi_k$ and $\varphi_{AC_k} = \phi'_{AC_k} - \phi_{AC_k}$, ($k = 1, 2, 3, 4$).

Similarly, by defining $|S, -1/2\rangle_1 |S, -1/2\rangle_2 \equiv |SS\rangle$, $|F, -1/2\rangle_1 |F, +7/2\rangle_2 \equiv |FF\rangle$, $|F, -1/2\rangle_1 |S, +1/2\rangle_2 \equiv |FS\rangle$, and $|S, -1/2\rangle_1 |F, +7/2\rangle_2 \equiv |SF\rangle$, the diagonal terms of the density matrix of the state $|B\rangle = |\psi'_B\rangle/\sqrt{2}$ becomes

$$\begin{aligned}
 \bullet |B\rangle\langle B| &= \frac{1}{2 \times 8} \\
 &\quad \times \left\{ [2 + 2 \cos(\psi + \Delta)] |SS\rangle\langle SS| + [2 + 2 \cos(\psi + \Delta)] |FF\rangle\langle FF| \right. \\
 &\quad \left. + [2 - 2 \cos(\psi + \Delta)] |FS\rangle\langle FS| + [2 - 2 \cos(\psi + \Delta)] |SF\rangle\langle SF| \right\} \\
 &= P_{SS} \cdot |SS\rangle\langle SS| + P_{DD} \cdot |FF\rangle\langle FF| + P_{DS} \cdot |FS\rangle\langle FS| + P_{SD} \cdot |SF\rangle\langle SF|,
 \end{aligned} \tag{2.26}$$

2.5. Scheme 3: Using a Mølmer Sørensen gate to produce fully entangled state

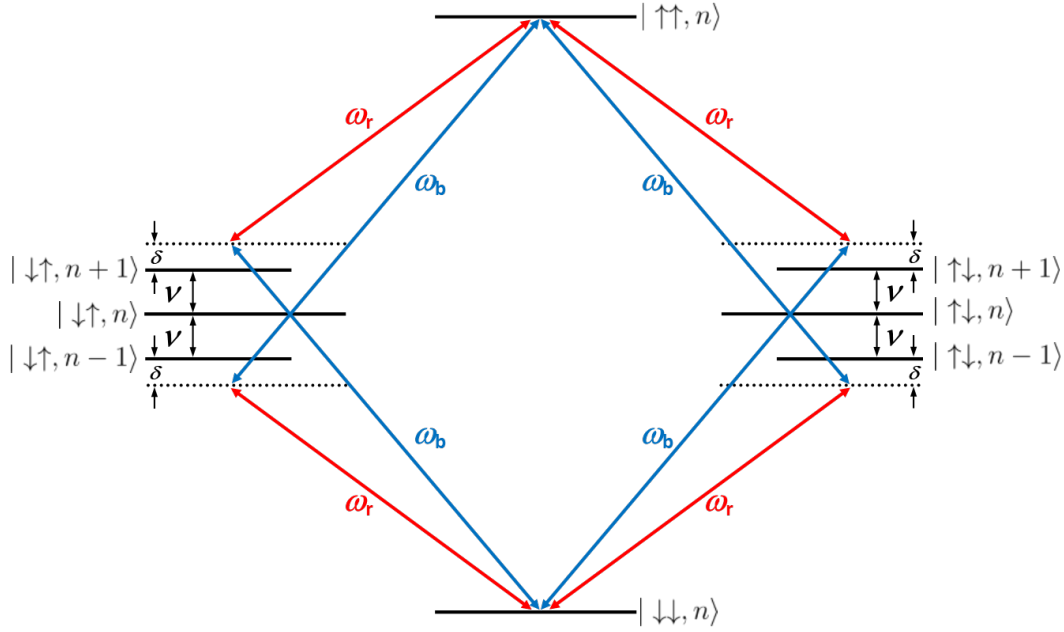


Figure 2.4.: The schematic drawing of the Mølmer Sørensen gate [26]. A bichromatic laser field with frequencies ω_b, ω_r satisfying $2\omega_0 = \omega_b + \omega_r$ is tuned close to the upper and lower motional sideband of the qubit transition ω_0 . ν is the secular frequency and δ is the detuning of the laser relative to the sidebands. The field couples the qubit states $|\downarrow\downarrow\rangle \leftrightarrow |\uparrow\uparrow\rangle$ via the four interfering paths shown.

where $\Delta := \varphi_4 + \varphi_{AC_4} + 2\varphi_2 + 2\varphi_{AC_2} - \varphi_1 - \varphi_{AC_1} - 2\varphi_3 - 2\varphi_{AC_3}$. Hence, the parity oscillation signal is

$$P = P_{SS} + P_{FF} - P_{FS} - P_{SF} = \frac{1}{2} \cos(\psi + \Delta). \quad (2.27)$$

2.5. Scheme 3: Using a Mølmer Sørensen gate to produce fully entangled state

To compensate for the losses of contrast, an effective way would be to create a fully entangled state instead of having a product state that dephases into a mixed state. One way of doing so is to use a Mølmer Sørensen gate [26–28] as shown in Fig. 2.4. As a starting point, the initial state is prepared to be $|S, -1/2\rangle_1 |S, -1/2\rangle_2$. The formula

2. Discussion on the Lorentz violation theory and detection schemes

of the state transformation in Fig. 2.4 is

$$|gg\rangle \rightarrow \cos\left(\frac{\tilde{\Omega}T}{2}\right)|gg\rangle + i\sin\left(\frac{\tilde{\Omega}T}{2}\right)|ee\rangle, \quad (2.28)$$

where $|g\rangle$ and $|e\rangle$ represents the ground state and the excited state, respectively.

When the Lamb-Dicke parameter and Rabi-frequency for the red and blue sideband is $\eta_1 = \eta_2 = \eta$ and $\Omega_1 = \Omega_2 = \Omega$ The effective Rabi frequency is defined as

$$\tilde{\Omega} = -\frac{(\Omega\eta)^2}{\nu - \delta}, \quad (2.29)$$

where Ω_0 is the carrier Rabi frequency, η is the Lamb-Dicke parameter, ν is the secular frequency, and δ is the detuning of the laser relative to the sidebands. With Eq. 2.28 and the gate time fulfilling $\tilde{\Omega}T = \pi/2$, the state becomes

$$\frac{1}{\sqrt{2}}(|S, -1/2\rangle_1|S, -1/2\rangle_2 + i|D, -3/2\rangle_1|D, -3/2\rangle_2). \quad (2.30)$$

Next, a $\pi/2$ -pulse with laser phase ϕ_L (transforms $|D, -3/2\rangle \leftrightarrow |S, -1/2\rangle$) is applied to obtain state $|A\rangle$

$$\begin{aligned} \bullet |A\rangle = \frac{1}{2\sqrt{2}} \Big\{ & [1 - ie^{2i(\phi_L + \phi_{AC})}] |S, -1/2\rangle_1|S, -1/2\rangle_2 \\ & + [i - e^{-2i(\phi_L + \phi_{AC})}] |D, -3/2\rangle_1|D, -3/2\rangle_2 \\ & + [e^{i(\phi_L + \phi_{AC})} - ie^{-i(\phi_L + \phi_{AC})}] |D, -3/2\rangle_1|S, -1/2\rangle_2 \\ & + [e^{i(\phi_L + \phi_{AC})} - ie^{-i(\phi_L + \phi_{AC})}] |S, -1/2\rangle_1|D, -3/2\rangle_2 \Big\}, \end{aligned} \quad (2.31)$$

where ϕ_{AC} is the AC-Stark shift induced by the $\pi/2$ -pulse. If $\phi_L + \phi_{AC} = -\pi/4 \Rightarrow 1 - ie^{2i(\phi_L + \phi_{AC})} = 0$, the state becomes

$$\bullet |A\rangle \rightarrow \frac{1}{2}(1 - i)(|D, -3/2\rangle_1|S, -1/2\rangle_2 + |S, -1/2\rangle_1|D, -3/2\rangle_2). \quad (2.32)$$

A π -pulse with laser phase ϕ_{L1} (transforms $|D, -3/2\rangle \leftrightarrow |S, +1/2\rangle$) is applied to produce the magnetic field protected state $|S, +1/2\rangle_1|S, -1/2\rangle_2 + |S, -1/2\rangle_1|S, +1/2\rangle_2$ for mapping to the ${}^2F_{7/2}$ manifold:

$$\bullet |B\rangle = \frac{1}{2}e^{i(\phi_{L1} + \phi_{AC_{L1}})}(-i - 1)(|S, +1/2\rangle_1|S, -1/2\rangle_2 + |S, -1/2\rangle_1|S, +1/2\rangle_2), \quad (2.33)$$

2.6. Scheme 4: Using dynamical decoupling to produce a mixture of Zeeman substates

and similarly the phase terms outside of the state brackets can be neglected such that

$$\bullet \quad |B\rangle \rightarrow \frac{1}{2}(-i-1)(|S, +1/2\rangle_1 |S, -1/2\rangle_2 + |S, -1/2\rangle_1 |S, +1/2\rangle_2). \quad (2.34)$$

Comparing Eq. 2.34 with Equ. 2.13, the only difference is that there is a factor $(-i-1)$. With the same method of mapping the state $|S, +1/2\rangle_1 |S, -1/2\rangle_2 + |S, -1/2\rangle_1 |S, +1/2\rangle_2$ to the corresponding ${}^2F_{7/2}$ Zeeman substates and extracting the LV signal, the parity oscillation signal P is also obtained and is

$$P = P_{SS} + P_{DD} - P_{DS} - P_{SD} = \cos(\psi + \Delta), \quad (2.35)$$

where $\Delta := \varphi_1 + \varphi_{AC_1} + \varphi_2 + \varphi_{AC_2} - \varphi_3 - \varphi_{AC_3} - \varphi_4 - \varphi_{AC_4}$.

The advantage of using a Mølmer Sørensen gate is as mentioned that a fully entangled state can be obtained and therefore the full contrast of the signal can be obtained. But the disadvantage is that it would potentially take longer to prepare an entangled state in the ${}^2S_{1/2}$ manifold.

2.6. Scheme 4: Using dynamical decoupling to produce a mixture of Zeeman substates

Scheme 1 to 3 suppress the magnetic field noise in the first order via exploiting quantum correlation and prepare the ions in an entangled state the average of the linear Zeeman shift being zero. However, the scaling of the numbers of ions with quantum correlation is limited and hard to obtain. Also laser induced AC-Stark shift may result in the decoherence of the state during the preparation process. A promising technique to implement dynamical decoupling in the ${}^2F_{7/2}$ manifold. With this method, less optical pulses are needed, no AC-Stark shift will be present due to radio-frequency (RF) operations, and measurements can be done with multiple ions. As discussed in [35], this method could potentially suppress the effect of the fluctuating magnetic field without a significant loss of sensitivity.

The Hamiltonian of the linear Zeeman effect is

$$\hat{\mathcal{H}}_{\text{lin}} = -\mu_z B_z \hat{J}_z, \quad (2.36)$$

where μ_z is the magnetic moment, $\mathbf{B} = B_z \hat{\mathbf{z}}$ is the weak external magnetic field and \hat{J}_z is the angular momentum operator component of $\hat{\mathbf{J}}$ in the $\hat{\mathbf{z}}$ direction with eigenvalues $m_j \hbar$, m_j has elements $-J$ to $+J$ in integer steps. Assume a small energy shift proportional to m_j^2 that can result from the second-order Zeeman shift, the electric

2. Discussion on the Lorentz violation theory and detection schemes

quadrupole shift caused by the inherent electric field gradient in the ion trap, and from possible LV signal. The Hamiltonian of this quadratic term can be written as

$$\hat{\mathcal{H}}_{\text{quad}} = \kappa \hat{J}_z^2. \quad (2.37)$$

Therefore, the free evolution Hamiltonian is

$$\begin{aligned} \hat{\mathcal{H}}_{\text{free}} &= \hat{\mathcal{H}}_{\text{lin}} + \hat{\mathcal{H}}_{\text{quad}} \\ &= -\mu_z B_z \hat{J}_z + \kappa \hat{J}_z^2. \end{aligned} \quad (2.38)$$

Assuming that the system can be driven with a RF oscillating magnetic field tuned close to the resonance frequency of the linear Zeeman splitting energy, such that

$$\omega_{\text{RF}} = \frac{\mu_z B_z}{\hbar} + \delta(t), \quad (2.39)$$

where $\delta(t)$ is caused by the fluctuation of magnetic field at the ion's position. The Hamiltonian of this time dependent coupling term is

$$\hat{\mathcal{H}}_{\text{coup}} = \Omega(t) \cos(\omega_{\text{RF}} t + \phi) \hat{J}_x, \quad (2.40)$$

where Ω is the multi-level Rabi frequency and ϕ is the RF phase. The total Hamiltonian is

$$\begin{aligned} \hat{\mathcal{H}}_{\text{total}} &= \hat{\mathcal{H}}_{\text{free}} + \hat{\mathcal{H}}_{\text{coup}} \\ &= -\mu_z B_z \hat{J}_z + \kappa \hat{J}_z^2 + \Omega(t) \cos(\omega_{\text{RF}} t + \phi) \hat{J}_x. \end{aligned} \quad (2.41)$$

By moving to the interaction picture with respect to the oscillating magnetic field, applying the rotating wave approximation, and assuming that $\Omega_0 \gg \kappa$, the evolution Hamiltonian becomes

$$\hat{\mathcal{H}}_{\text{total}} \rightarrow -\delta(t) \hat{J}_z + \kappa \hat{J}_z^2 + \Omega(t) [\hat{J}_x \cos(\phi) - \hat{J}_y \sin(\phi)]. \quad (2.42)$$

The dynamical decoupling method aims to measure κ while ignoring the unwanted magnetic field noise $\delta(t)$ by a periodic modulation of Ω and ϕ . The scheme sequence performs as below and is visualized in Fig. 2.5:

1. Fig. 2.5a: the ion is initialized to a spin state \hat{J} in a specific \hat{J}_z eigenstate $|J, m_j = m'\rangle$;
2. Fig. 2.5b: a resonant pulse with duration of $\tau = \pi/(2\Omega_0)$ ($\pi/2$ -pulse) and with phase defined as $\phi = 0$ is applied. The evolution operator is $e^{i(\pi \hat{J}_x/2)}$ and this maps the spin state to the corresponding J_y eigenstate, i.e. it acts as the first $\pi/2$ -pulse of a Ramsey sequence [36];

2.6. Scheme 4: Using dynamical decoupling to produce a mixture of Zeeman substates

3. Modulation sequence: (numbers in the bracket is the corresponding subgraphs in Fig. 2.5)

$$[t_\omega] \text{ (2.5c)} \rightarrow [\pi_{+y}] \text{ (2.5d)} \rightarrow [2t_\omega] \text{ (2.5e)} \rightarrow [\pi_{-y}] \text{ (2.5f)} \rightarrow [t_\omega] \text{ (2.5g)} \quad (2.43)$$

where t_ω is the waiting time between pulses where the spin evolves freely. It is chosen such that during the $4t_\omega$ time, the magnetic field fluctuation $\delta(t)$ changes slowly and is effectively constant. $\pi_{\pm y}$ are RF pulses with duration of π/Ω_0 with $\phi = \pm\pi/2$. The phase $\phi = \pm\pi/2$ gives a $\pm 90^\circ$ shift for the starting point of the pulse on the equator as shown in Fig. 2.5d and 2.5f;

4. n repetitions of the modulation sequence. The phase $\phi = \pi$ of the second RF $\pi/2$ -pulse in the next step is chosen such that the Ramsey fringe has a maximal sensitivity to a possible LV signal [35]. One repetition of the modulation sequence brings the population of the state to point **B**. An even number of repetitions brings the population of the state to point **A**. In order to bring the population back to the initialized $|J, m_j = m'\rangle$ state by means of a second RF $\pi/2$ -pulse with an phase $\phi = \pi$, an even number of repetition n is required;
5. Fig. 2.5h: a second RF $\pi/2$ -pulse is applied with a phase $\phi = \pi$ with respect to the first RF $\pi/2$ -pulse to bring the population of the state back to the initialized $|J, m_j = m'\rangle$ state.

At step 3, the evolution operator of the spin system during the modulation sequence is

$$\hat{\mathcal{U}} = e^{i(-\delta t_\omega \hat{J}_z + \kappa t_\omega \hat{J}_z^2)} \cdot e^{i(-\pi \hat{J}_y)} \cdot e^{i(-2\delta t_\omega \hat{J}_z + 2\kappa t_\omega \hat{J}_z^2)} \cdot e^{i(+\pi \hat{J}_y)} \cdot e^{i(-\delta t_\omega \hat{J}_z + \kappa t_\omega \hat{J}_z^2)}. \quad (2.44)$$

With the commutation relation $[\hat{J}_z^2, e^{i(\pm\pi \hat{J}_y)}] = 0$, the signal term $\kappa \hat{J}_z^2$ generates a phase shift which is coherently accumulated during the sequence. Since $[\hat{J}_z, e^{i(\pm\pi \hat{J}_y)}] \neq 0$, the phase due to the magnetic field noise term $\delta(t)J_z$ is largely reduces by averaging. The operation $e^{i(-\pi \hat{J}_y)} \cdot A \cdot e^{i(+\pi \hat{J}_y)}$ acts as a π rotation of the operator A around the \hat{y} axis, and this transforms $+\hat{J}_z$ to $-\hat{J}_z$, i.e.

$$e^{i(-\pi \hat{J}_y)} \cdot e^{i(-2\delta t_\omega \hat{J}_z + 2\kappa t_\omega \hat{J}_z^2)} \cdot e^{i(+\pi \hat{J}_y)} \rightarrow e^{i(+2\delta t_\omega \hat{J}_z + 2\kappa t_\omega \hat{J}_z^2)}, \quad (2.45)$$

and the evolution operator $\hat{\mathcal{U}}$ in the approximation of the slowly varying $\delta(t)$ becomes $e^{i(4\kappa t_\omega \hat{J}_z^2)}$ and the phase due to the linear Zeeman effect cancels out. And with n repetitions in step 4 with total time of $T = 4nt_\omega$, the evolution from the modulation sequence becomes $\hat{\mathcal{U}} = e^{i(\kappa T \hat{J}_z^2)}$. The evolution operator of the entire sequence is

$$\hat{\mathcal{U}} = e^{i(-\frac{\pi}{2} \hat{J}_x)} \cdot e^{i(\kappa T \hat{J}_z^2)} \cdot e^{i(\frac{\pi}{2} \hat{J}_x)} \quad (2.46)$$

2. Discussion on the Lorentz violation theory and detection schemes

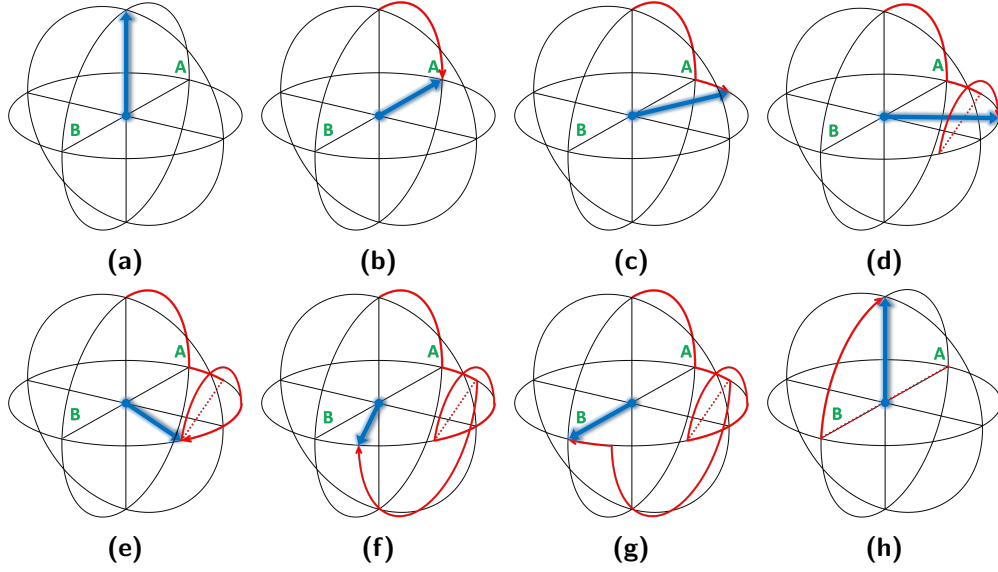


Figure 2.5.: The visualization of scheme 4. (a) Ion is initialized to a specific state $|J, m_j = m'\rangle$. (b) A resonant RF $\pi/2$ -pulse with $\phi = 0$ maps the spin state to the corresponding \hat{J}_y eigenstate. (c) A free evolution time t_ω . (d) A π -pulse with $\phi = +\pi/2$. (e) A free evolution time $2t_\omega$. (f) A π -pulse with $\phi = -\pi/2$. (g) A free evolution time t_ω . (h) A second RF $\pi/2$ -pulse with $\phi = \pi$. The phase value of the second RF $\pi/2$ -pulse is chosen such that the Ramsey fringe has a maximal sensitivity to a possible LV signal [35]. One repetition of the modulation sequence brings the population of the state to point **B**, and even numbers of repetitions bring the population of the state to point **A**. In order to bring the population back to the initialized $|J, m_j = m'\rangle$ state with a second RF $\pi/2$ -pulse having a phase $\phi = \pi$, even number of repetition n is required.

2.7. Sensitivity estimations and comparison of scheme 1-4

where the phase of the last $\pi/2$ -pulse can be used to account for any systematic constant imbalance between wait times that could arise from experimental imperfection.

Finally, the population in the initial state, $P_{J,m'}(\kappa T, \phi) = |\langle J, m' | \hat{\mathcal{U}} | J, m' \rangle|^2$, is measured. To extract the possible LV signal, the results of sequential measurements in time of $P_{J,m'}(\kappa T, \phi)$ is monitored and fitted to the model expressed mathematically as Eq. 2.6 to see if there is any oscillation signal referring to the theoretical sidereal day.

We want to interrogate the transition which has the least sensitivity to magnetic field, i.e. the smallest linear Zeeman shift. This is the $|S, -1/2\rangle \leftrightarrow |F, -1/2\rangle$ transition with a Zeeman sensitivity of 0.60 MHz/G. The operation of the scheme with $^{172}\text{Yb}^+$ ions is as follows:

1. $^{172}\text{Yb}^+$ ions are optically pumped to $|S, -1/2\rangle$;
2. Excite the ions to the initial experimental state $|F, -1/2\rangle$ with a π -pulse of 467 nm laser;
3. The first RF $\pi/2$ -pulse with Ω_0 is performed such that all the Zeeman substates are coupled and populated. Ω_0 is the Rabi frequency corresponding to the Zeeman splitting energy;
4. Apply the modulation sequence with even number of n repetitions;
5. The second RF $\pi/2$ -pulse is applied to close the sequence;
6. Monitor the state population of $|F, -1/2\rangle$ in time to see if there is any oscillation of the population corresponding to a possible LV signal.

2.7. Sensitivity estimations and comparison of scheme 1-4

The upper bound limit of the Lorentz violation parameter $\Delta C_0^{(2)}$ provided by the SME theory with the method exploiting quantum correlation has been estimated in [30]. To know if the method with dynamical decoupling is comparable to using quantum correlation, the sensitivity of it needs to be estimated. In this section, the sensitivity of the different method will be estimated and compared.

The precision of the measurement is given by $\Delta\kappa$ [35]. For scheme 3 [30], where a fully entangled pair of Yb^+ ions is assumed, $\Delta\kappa$ can be calculated using [35]

$$\Delta\kappa = 0.083 \frac{\text{rad}}{N\sqrt{\tau T}}, \quad (2.47)$$

2. Discussion on the Lorentz violation theory and detection schemes

where T , τ , and N are the Ramsey time, total integration time, and the number of spin probes, correspondingly. By comparing Eq. 2.4 to Eq. 2.47, one can calculate the precision $\Delta C_{0\text{QC}}^{(2)}$ [37]:

$$\frac{\Delta E}{h} = (m_{j_2}^2 - m_{j_1}^2) \cdot \frac{\Delta \kappa}{2\pi} = 5.11 \times 10^{15} \text{ Hz} \cdot (m_{j_2}^2 - m_{j_1}^2) \cdot \Delta C_{0\text{QC}}^{(2)}. \quad (2.48)$$

Therefore, $\Delta C_{0\text{QC}}^{(2)}$ is

$$\Delta C_{0\text{QC}}^{(2)} = \frac{0.083 \frac{\text{rad}}{N\sqrt{\tau T}}}{2\pi} \times \frac{1}{5.11 \times 10^{15}} = \frac{2.58 \times 10^{-18}}{N\sqrt{\tau T}}. \quad (2.49)$$

Due to the fact that only 50% of the mixed state is in the entangled state in scheme 1 and 2, $\Delta C_{0\text{QC}}^{(2)}$ would be a factor of 2 larger than scheme 3 where a fully entangled ion pair is discussed.

For scheme 4, $\Delta \kappa$ is [35]

$$\Delta \kappa = 0.1 \frac{\text{rad}}{\sqrt{N\tau T}}, \quad (2.50)$$

and $\Delta C_{0\text{DD}}^{(2)}$ can be calculated as

$$\Delta C_{0\text{DD}}^{(2)} = \frac{3.11 \times 10^{-18}}{\sqrt{N\tau T}}. \quad (2.51)$$

The smaller the value of $\Delta C_0^{(2)}$, the more sensitive the experiment is to the signal of a possible LV. From the equation, we see that the sensitivity with fully entangled ions via quantum correlation is $\Delta C_{0\text{QC}}^{(2)} \propto 2.58/N$ which scales down with the number of ions N , $\Delta C_{0\text{DD}}^{(2)} \propto 3.11/\sqrt{N}$. Therefore, with no experimental limitations, quantum correlation method would be better. However, due to the fact that the scaling of ion numbers with quantum correlation is much harder than with dynamical decoupling and that the coherence time decreases with the increasing number of ions, dynamical decoupling would be easier and more straight forward.

A list of calculated sensitivities via dynamical decoupling with different interrogation time, total averaging time, and ion numbers can be found in Table 2.1 and 2.2. From the estimation, it can be seen that with 2 ions, the sensitivity of 8.1×10^{-21} can already be reached in 24h of integration time.

2.7. Sensitivity estimations and comparison of scheme 1-4

Number of ions/Interrogation time T	$T=0.1$ s	$T=1$ s	$T=10$ s
2	2.4×10^{-20}	7.4×10^{-21}	2.4×10^{-21}
5	1.5×10^{-20}	4.7×10^{-21}	1.5×10^{-21}
10	1.1×10^{-20}	3.3×10^{-21}	1.1×10^{-21}

Table 2.1.: Table of sensitivity $\Delta C_0^{(2)}$ for a total averaging time of 24 h. The number of ions in an ion chain is chosen as 2, 5, and 10. The interrogation time is chosen to be 0.1 s, 1 s, and 10 s.

Number of ions/Interrogation time T	$T=0.1$ s	$T=1$ s	$T=10$ s
2	1.1×10^{-20}	3.3×10^{-21}	1.1×10^{-21}
5	6.7×10^{-21}	2.1×10^{-21}	6.7×10^{-22}
10	4.7×10^{-21}	1.5×10^{-21}	4.7×10^{-22}

Table 2.2.: Table of sensitivity $\Delta C_0^{(2)}$ for a total averaging time of 5×24 h. The number of ions in an ion chain is chosen as 2, 5, and 10. The interrogation time is chosen to be 0.1 s, 1 s, and 10 s.

3. Experimental setup

This chapter discusses the experimental setup for the test of LV. First, the octupole laser source to be implemented in the LV experiment is introduced. This is the laser light that is shared with PTB's $^{171}\text{Yb}^+$ single-ion optical clock. Then the setup of the 934 nm laser breadboard used for bridging the frequency of the two Yb^+ isotopes will be shown, in particular the slave diode lasers for intensity enhancement, the high frequency (HF) acousto-optic modulator (AOM) for bridging the frequency difference of the two Yb^+ isotopes, and the sealed slave. Next, the 467 nm laser breadboard for frequency doubling and scanning of the octupole laser will be shown with particular interest on the second-harmonic-generation (SHG) waveguide.

3.1. The octupole laser for the $^{171}\text{Yb}^+$ single-ion optical clock

In order to interrogate the octupole transition in $^{172}\text{Yb}^+$, a fractional amount of the laser light ($\approx 8\text{ mW}$) at 934 nm used in the single-ion $^{171}\text{Yb}^+$ clock at PTB is shared. The laser light is transferred to the $^{172}\text{Yb}^+$ ion experiment via a telecommunication fiber link between the two buildings Kopfermann-Bau and Giebe-Bau. The frequency difference between the two different isotopes of Yb^+ ions is 4711.5 MHz with an uncertainty of 700 kHz [33].

As shown in Fig. 3.1, most of the laser light at 934 nm in Kopfermann-Bau is used for the single-ion $^{171}\text{Yb}^+$ clock. The frequency of it, denoted by $\nu_{934\text{ nm}}$ in Fig. 3.1, is shifted by an AOM by +80 MHz and frequency doubled with a SHG waveguide. A double-pass AOM is then used to sweep the frequency of the laser light for the interrogation of the octupole transition in $^{171}\text{Yb}^+$.

The source of the $\nu_{934\text{ nm}}$ laser light is an external-cavity diode laser (ECDL). It is first locked to an ultra-low-expansion (ULE) cavity as a short term reference such that the instability of the laser reaches a level of 10^{-16} in a second. A second stabilization stage is realized by referencing the frequency of the laser to the silicon cavity [38] at Paschen-Bau via a frequency comb. The instability of the laser then reaches a level of 5×10^{-17} within seconds of averaging time. The frequency of the 934 nm laser is $\nu_{934\text{ nm}} = 321\,060\,742.386\,322\,5\text{ MHz}$ with an uncertainty at sub-hertz level.

3. Experimental setup

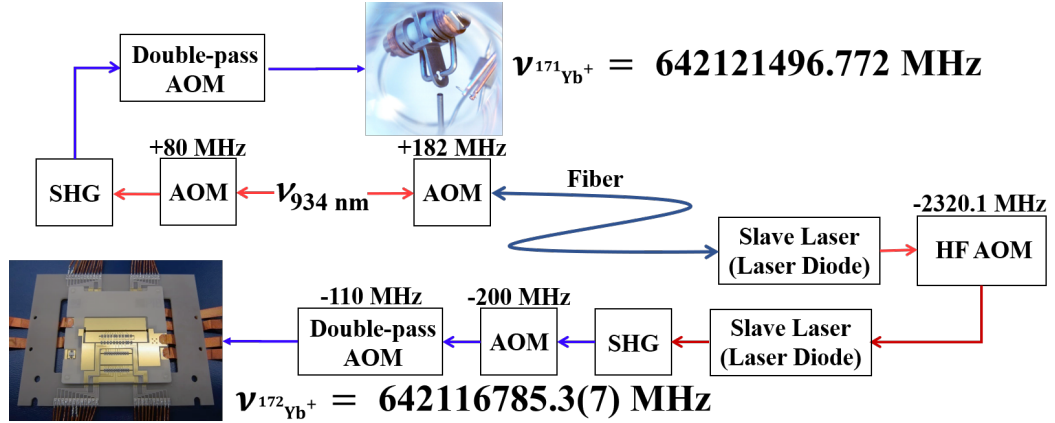


Figure 3.1.: Schematic overview of laser light preparation for the interrogation of the octupole transition of $^{172}\text{Yb}^+$. The frequency of the small fractional amount of laser light transferred to the $^{172}\text{Yb}^+$ LV experiment is $\nu_{934\text{ nm}} = 321\,060\,924.742\,322\,5\text{ MHz}$ with an uncertainty at hundred hertz level. The instability of the laser reaches a level of 5×10^{-17} within seconds of averaging time. The frequency difference between the two different isotopes of Yb^+ ions is 4711.5 MHz with an uncertainty of 700 kHz [33].

A small fraction of this laser light at 934 nm is frequency shifted by +182 MHz and sent through the telecommunication fiber to the $^{172}\text{Yb}^+$ experiment, arriving at the 934 nm breadboard. This same AOM is used for fiber phase stabilization together with another AOM (this AOM is not shown in Fig. 3.1) at the output port of the fiber. The zeroth order of the AOM at the output port of the fiber is used as the injection laser for the first slave laser and the -1^{st} -order is sent back with a mirror through the fiber for fiber phase stabilization.

3.2. 934nm breadboard

Fig. 3.2 shows the schematic setup of the 934 nm breadboard. The laser light from Kopfermann-Bau exits the fiber holder with $\approx 1\text{ mW}$ of optical power. In order to have enough power at 467 nm for the interrogation of the octupole transition, two slave diode lasers (SDL) are implemented. First, the Kopfermann-Bau laser is injected into the first SDL, which enhances the power to $\approx 50\text{ mW}$. The enhanced light passes through an AOM that shifts the frequency of the laser by 2320.1 MHz. The -1^{st} -order of the AOM is injected into a second SDL for another power enhancement before transferring it into the waveguide for frequency doubling.

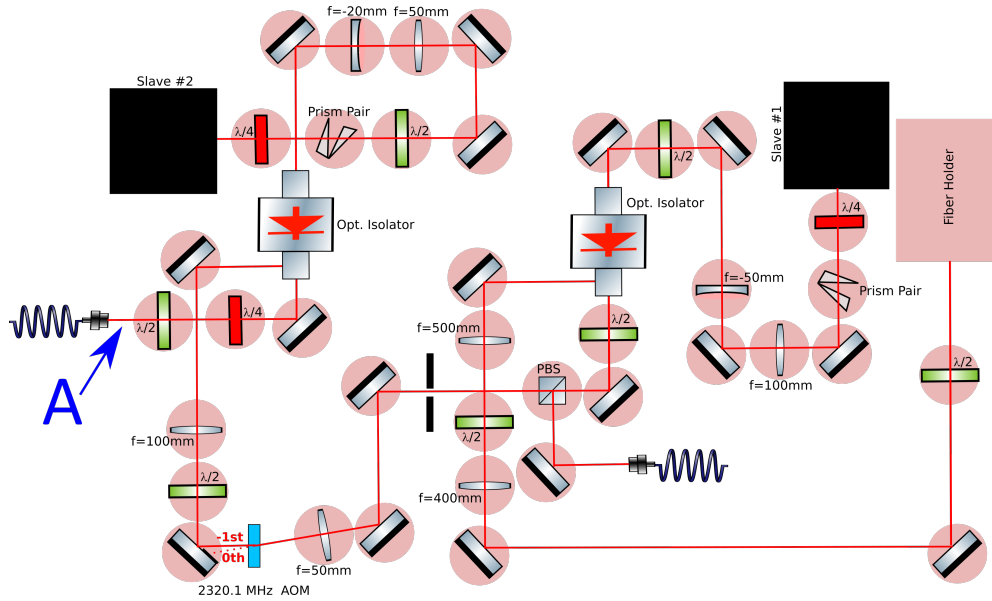


Figure 3.2.: Schematic drawing of the 934 nm breadboard. The fiber transferring the laser light from the $^{171}\text{Yb}^+$ optical clock is mounted in a rigid fiber holder. Two slave diode lasers (SDL) are used on this breadboard. A HF AOM that shifts the frequency of the laser by 2320.1 MHz is implemented to bridge the frequency gap between the two Yb^+ isotopes. A typical optical power of 155 mW is measured at point A. The fiber transfers the laser light to the SHG waveguide.

3.2.1. Slave diode lasers

In order to increase the intensity of a laser while maintaining its spectral properties, it is often essential to build a high-power SDL. The laser diode used in the slave is a high power single mode laser diode¹. It has a maximum optical output power of 300 mW and an operating temperature range from -10°C to 30°C . With a fixed optical output power, the center of the optical spectrum shifts as the temperature changes as is shown in Fig. 3.3. In the figure, the optical spectra of a free-running SDL at two different temperatures are recorded with an optical spectrum analyzer (OSA). The operating current is fixed at 200 mA. As can be seen, the center of the spectrum is shifted to lower wavelength as the temperature of the SDL is decreased. At 20.8°C , the center of the spectrum is around 941 nm; at 17.6°C , the center of the spectrum is around 939 nm. This means

¹Toptica #LD-0940-0300-1

3. Experimental setup

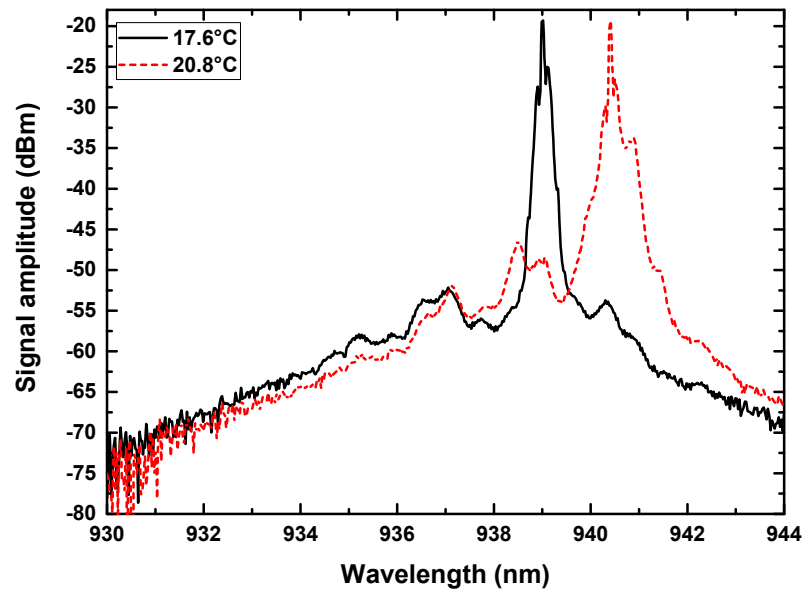


Figure 3.3.: Optical spectrum of a free-running SDL with an operating current of 200 mA at different temperatures. The center of the spectrum shifts from 941 nm to 939 nm as the temperature decreases from 20.8°C (red, dashed line) to 17.6°C (black, solid line).

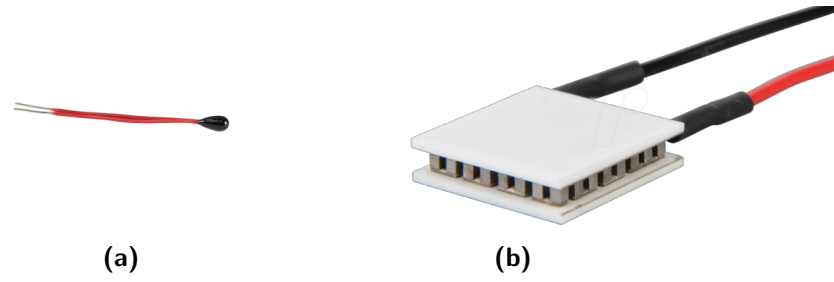


Figure 3.4.: Elements for temperature control. (a) Thermistor. (b) Peltier element.

that at lower temperatures, the center of the spectrum is closer to 934 nm, and a lesser optical injection power at 934 nm is needed in order to lock the SDL at 934 nm. For temperature stabilization of the SDL, a thermistor² (Fig. 3.4a) and peltier element³ (Fig. 3.4b) connected to a temperature controller⁴ is used.

After assembling the SDL, the laser needs to be collimated. This is done by altering the distance between the laser diode and the lens as can be seen in Fig. 3.5. The beam profile of the laser beam produced by this laser diode is elliptical, and the measured ellipticity is 9:1. To manipulate the beam profile such that it is circular and almost Gaussian, an arrangement of two anamorphic prisms is needed. A schematic drawing of the prism pair is shown in Fig. 3.6. With the prism pair, the ratio of the horizontal waist by the vertical waist changes from 9:1 to 4.5:1. To make the beam even closer to a symmetric Gaussian beam, cylindrical lenses with focal lengths being +100 mm and -50 mm are used for the first SDL and cylindrical lenses with focal lengths being +50 mm and -20 mm are used for the second SDL as shown in Fig. 3.2.

One example of the SDL being locked to the master laser is shown in Fig. 3.7. The figure shows the optical spectrum of the laser diode taken with an OSA. The red, solid line represents the spectrum of the free-running laser diode and the black, solid line represents the spectrum when the master laser is injected. As can be seen, when the temperature is not optimized, the laser diode will not lock to the master laser. The blue, solid line represents the spectrum when the master laser is injected and the temperature of the laser diode is optimized (the temperature is lowered). When the SDL is locked to the master laser, the suppression obtained is ≈ 40 dB.

²Thorlabs TH10K

³Thorlabs TEC3-2.5

⁴Thorlabs TED200C

3. Experimental setup

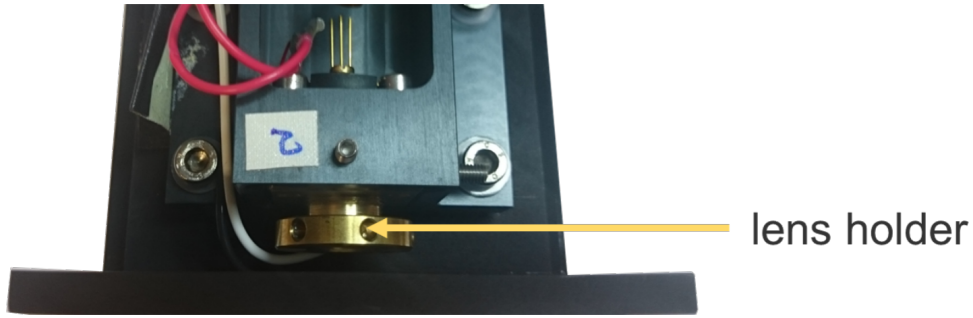
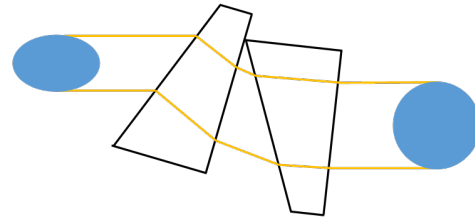


Figure 3.5.: The assembled SDL. With an allen key, the lens holder can be adjusted for laser beam collimation.

Figure 3.6: The anamorphic prism pair. It scales down one axis or magnifies it depending on the propagating direction of the laser beam. The orange lines are a sketch to get an intuition for the beam path.



3.2.2. High frequency AOM

Fig. 3.8a shows the HF AOM⁵ used to shift the frequency of the 934 nm laser by 2320.1 MHz. The AOM is glued to a homemade mount that can rotate and tilt for the alignment of the AOM with respect the incident beam. The source of the AOM is created by a PTB-made DDS synthesizer which generates 2320.1 MHz and is amplified with an amplifier⁶ to 30 dBm signal output power. The source is referenced to a 10 MHz maser signal. The AOM can withstand a maximum incident laser power of 50 mW with a waist of 37.5 μm and has a -1^{st} -order diffraction efficiency of 1.3 %.

3.2.3. Sealed slave

With 50 mW of incident laser power and a -1^{st} -order diffraction efficiency of 1.3 % for the AOM, the -1^{st} -order diffraction output power of the AOM is 650 μW . This power is so low that the frequency-doubled 467 nm laser power after the waveguide will not be enough to interrogate the octupole transition. Therefore, a second SDL is implemented to enhance the power of the frequency-shifted 934 nm laser. The -1^{st} -order diffraction beam of the HF AOM acts as the injection laser for the second SDL. To obtain tens of mW of power at 467 nm at the ion, the input beam of the waveguide (measured at

⁵Brimrose, GPF-2360-100-934

⁶Qorvo, TQP9111

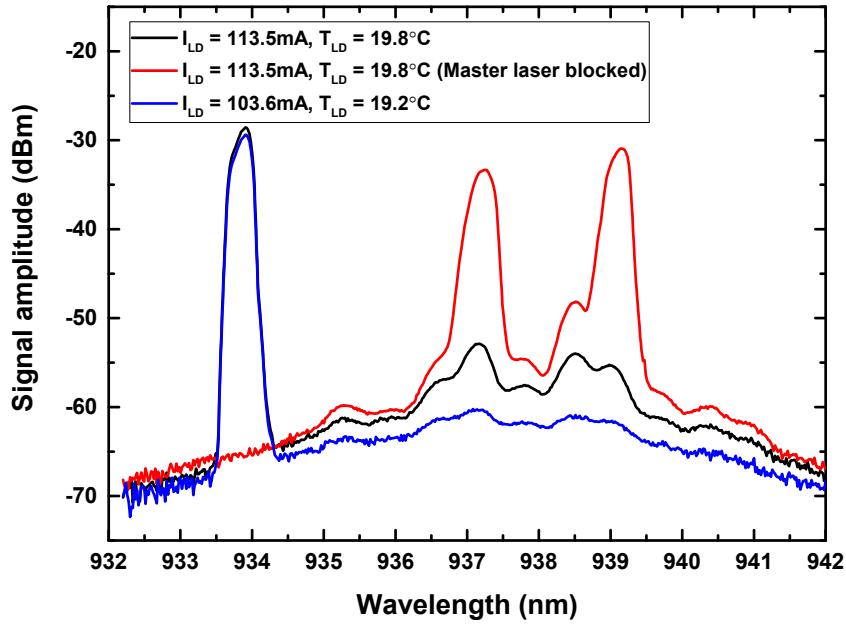


Figure 3.7.: Optical spectrum of the laser diode. A free-running laser diode would have a spectrum centered around 938 nm as shown with the red line, and the laser diode seeded with the master laser would have a center at 934 nm. Without optimized temperature of the laser diode, the SDL would not lock to the injected master laser, the spectrum of it is the black line. When the temperature is optimized and the amount of injection power for the master laser is above the minimum value, the SDL locks to the master laser and the spectrum looks like the blue line.

3. Experimental setup

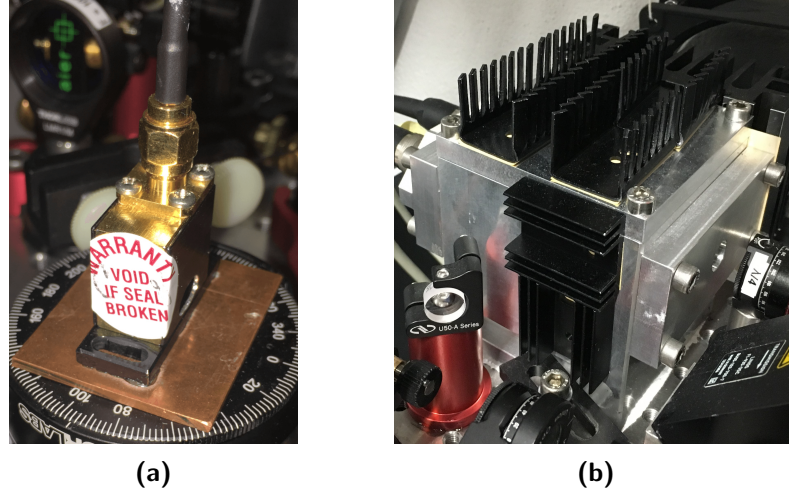


Figure 3.8.: (a) 2320.1 MHz HF AOM for bridging the frequency between the two Yb^+ isotopes. This AOM has 1.3 % of -1^{st} -order diffraction efficiency. (b) The sealed slave with heat sinks stuck to the surface of the housing via heat conducting tape.

point A as shown in Fig. 3.2) needs to be more than 100 mW. After all the optical elements, the injection power for the second SDL is 550 μW . Due to limited injection power, the temperature of the SDL needs to be stabilized at a lower point (lower than the room temperature) so that the amount of injection power needed for the SDL to be locked decreases. To be able to decrease the stabilized temperature without damaging the laser diode due to air moisture, a laser housing has been manufactured by Martin Menzel, a co-worker from PTB. The laser housing is mechanically sealed and filled with Argon gas so that there is no air moisture inside the housing as shown in Fig. 3.8b. The Argon gas is inexpensive, non-toxic, colorless, and odorless. It can be used in all climates and is favored in this situation. Several heat sinks are attached to the laser housing in order to release the heat inside the housing such that the temperature can be stabilized below the room temperature.

The relation between the resistance of the thermistor in $\text{k}\Omega$ and the stabilized temperature of the sealed SDL in $^{\circ}\text{C}$ is shown in Fig. 3.9. This shows that the larger the resistance of the temperature controller, the lower the stabilized temperature of the SDL. The temperature of the diode laser is measured by first putting a temperature sensor inside the housing, then the laser housing is filled with Argon gas. The SDL is closed with plastic screws and rubber gaskets.

Several SDL locking points have been tested and are shown in Fig. 3.10, where the

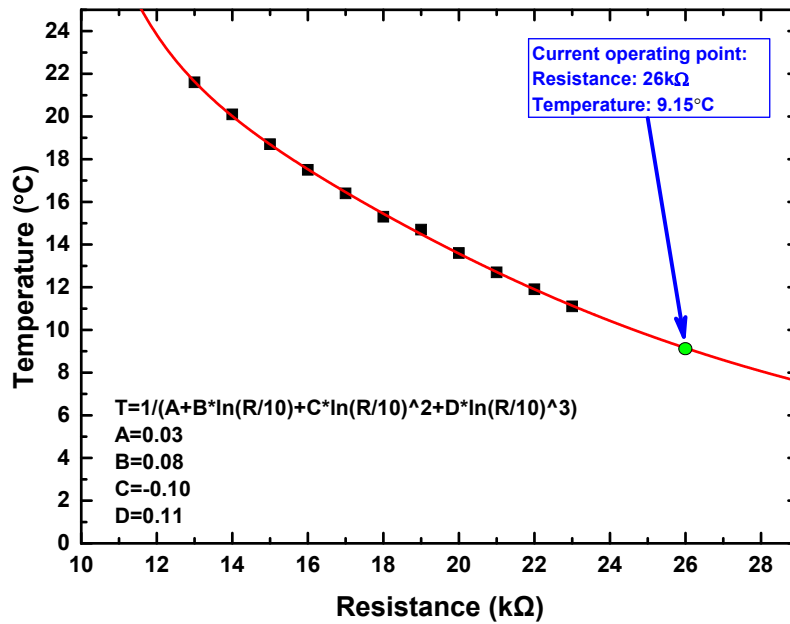
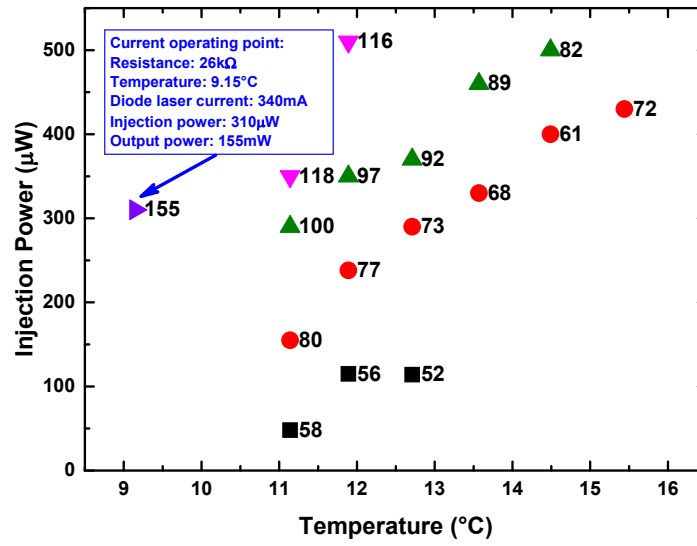
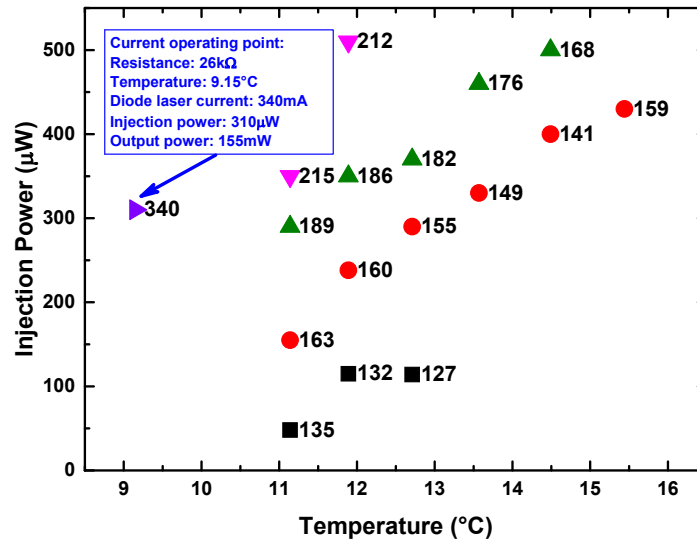


Figure 3.9.: The temperature of the sealed SDL in °C vs. the resistance of the thermistor in kΩ. The fitted equation for the relation between the resistance (R) and the temperature (T) is $T = 1 / [A + B \times \ln(R/10) + C \times \ln(R/10)^2 + D \times \ln(R/10)^3]$ with A , B , C , and D being values in the figure.

3. Experimental setup



(a)



(b)

Figure 3.10.: The injection power of the sealed SDL in μ W vs. the temperature of the laser diode in $^{\circ}$ C. (a) The bold font number beside each measurement point is the output power of the SDL in units of mW measured at point A in Fig. 3.2. (b) The bold font number beside each measurement point is the operating current of the SDL in units of mA.

\hat{x} -axis is the temperature of the laser diode in units of $^{\circ}\text{C}$ and the \hat{y} -axis is the minimum injection power at that temperature in units of μW . Each experimental point corresponds to a measurement done by first setting and stabilizing the temperature, then finding the minimum injection power. The bold font number beside each measurement point in Fig. 3.10a is the output power of the SDL in units of mW measured at point A in Fig. 3.2. In Fig. 3.10b, the bold font number is the operating current of the diode laser in units of mA. The measurement points are sorted with different colors and shapes, this shows a pattern that by increasing the resistance, i.e. lowering the stabilized temperature, the minimum injection power decreases and a higher output power can be achieved. Due to limited speed of heat transport inside the sealed box, the SDL is not able to stabilize at a temperature below 9°C . Together with the limited amount of injection power of $550\mu\text{W}$, the typical operating values for the second SDL is chosen as $T = 9.15^{\circ}\text{C}$ (corresponding to a resistance of $26\text{k}\Omega$ for the temperature controller) with a operating current of 340mA . With a minimum injection optical power of $310\mu\text{W}$, the SDL gives an optical output power of 155mW .

3.3. 467nm SHG breadboard

Fig. 3.11 is the schematic drawing of the 467 nm breadboard. The enhanced 934 nm laser light after the sealed SDL is guided into the SHG waveguide⁷ via two polarization maintaining (PM) fibers. The SHG waveguide is shown in Fig. 3.12. It frequency doubles the 934 nm laser light into 467 nm. An optimal temperature for the waveguide needs to be set to obtain maximal frequency doubling efficiency. To stabilize the temperature of the waveguide, it is also connected to a Thorlabs TED200C temperature controller. The typical temperature for maximal efficiency is $\approx 40^{\circ}\text{C}$ which corresponds to $5.318\text{k}\Omega$ of resistance for the thermistor. The first PM fiber has a coupling efficiency of 62 % and the fiber connector has a transmission efficiency of 86 %. To increase the stability of the laser light, an additional intensity stabilization is acting on a 200 MHz AOM. The stability reaches 5×10^{-3} on minute time scale. A double-pass AOM at 110 MHz is used for fine-tuning of the laser frequency to the resonance of the octupole transition.

The output power of the waveguide vs. the 934 nm laser power input is shown in Fig. 3.13. In the figure, the \hat{x} -axis is the output of the SDL before coupling into the waveguide fiber in units of mW, and the \hat{y} -axis is the output power of the waveguide in units of mW. The red square points are measurements done with a single PM fiber of 62 % transmission rate. In the final setup, two fibers are used and are connected with a fiber connector. Therefore, after taking into account the transmission rate of the

⁷NEL WH-0467-000-A-B-C

3. Experimental setup

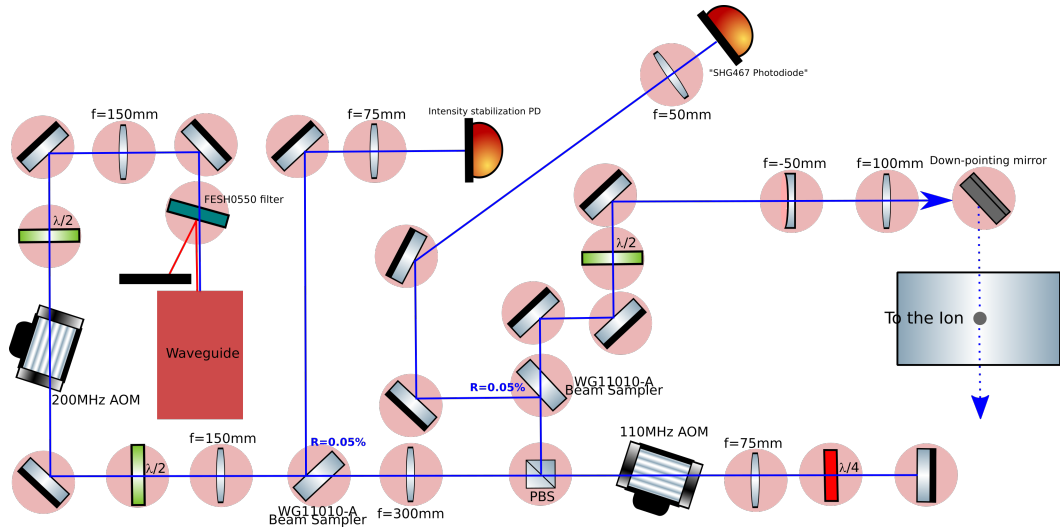


Figure 3.11.: Schematic setup of the 467 nm breadboard. A waveguide is implemented for frequency doubling together with a AOM that shift the frequency of the laser by 200 MHz and a double-pass AOM of 110 MHz. The 200 MHz AOM is also used as the AOM for intensity stabilization of the laser light. The frequency of the 110 MHz double-pass AOM is varied for the interrogation of the octupole transition. The typical optical power at the ion is 12 mW.

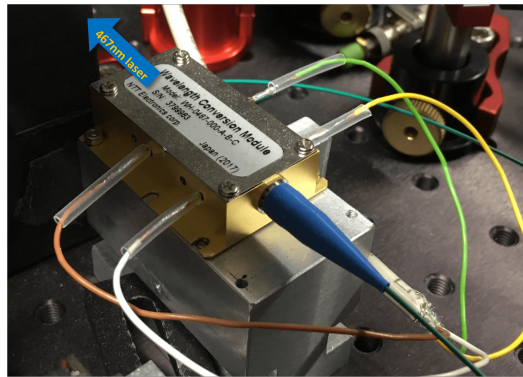


Figure 3.12.: The SHG waveguide. It frequency doubles the 934 nm laser light into 467 nm. A temperature of 40 °C for the waveguide needs to be set to obtain maximal frequency doubling efficiency.

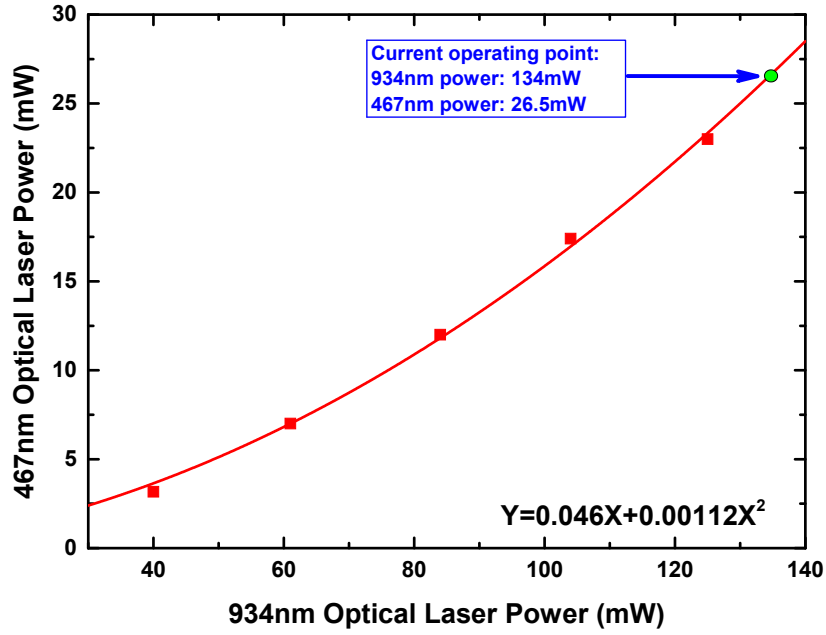


Figure 3.13.: The output power of the waveguide vs. the 934nm laser power. The red dots are the measured values and the red solid line is the fitted parabola with a fit function being $Y = 0.046X + 0.00112X^2$.

fiber connector of 86 %, the 155 mW of output power of the sealed SDL corresponds to 134 mW in Fig. 3.13. The value 134 mW verifies the fitted equation in Fig. 3.13. With an output power of the second SDL, the typical output power of the waveguide at 467 nm is 26.5 mW. After passing through the 200 MHz AOM with 88 % of -1^{st} -order transmission efficiency and the double-pass AOM with 66 %, the laser power at the position of the ion is ≈ 12 mW.

4. Octupole transition of a single $^{172}\text{Yb}^+$ ion

At the beginning of this chapter, the octupole selection rules are discussed. They are used to calculate the Rabi frequency and the π -pulse time of the octupole transition. The laser beam properties and the alignment procedure of the 467 nm octupole laser are shown, followed by the pulse sequence we will use to interrogate the octupole transition.

4.1. Octupole selection rules

The $^2S_{1/2} \leftrightarrow ^2F_{7/2}$ transition probability is spread over 14 Zeeman components of $\Delta m_J = 0, \pm 1, \pm 2, \pm 3$ in the presence of an external magnetic field. To obtain a maximal excitation probability to the desired Zeeman substates, the relation between the direction of the magnetic field, the wave vector of the 467 nm octupole laser beam, and the polarization of the laser need to be set such that the relative intensities of the Zeeman components are maximized. The coordinate system is visualized in Fig. 4.1, where θ is the angle between the wave vector of the laser light \mathbf{k} and the magnetic field \mathbf{B} , ϕ is the angle that the polarization of the laser light \mathbf{e} is tipped out of the plane of \mathbf{k} and \mathbf{B} . The relation between the relative intensities, direction of the magnetic field, the laser wave vector, and the polarization of the laser is given by [39]

$$I(m_J \rightarrow m'_J) \propto R_{|m_J - m'_J|} \begin{pmatrix} 7/2 & 3 & 1/2 \\ m'_J & m_J - m'_J & -m_J \end{pmatrix}^2, \quad (4.1)$$

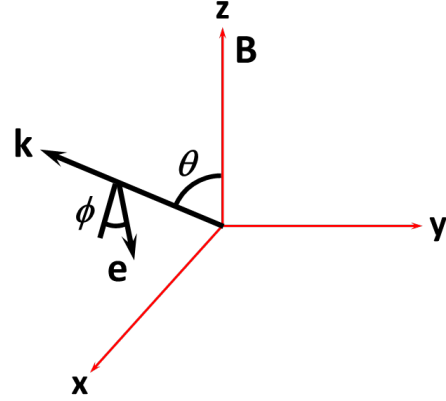
with

$$\begin{aligned} R_0 &= 12 \sin^2 \theta \cos^2 \phi (1 - 5 \cos^2 \theta)^2 \\ R_1 &= \cos^2 \theta \cos^2 \phi (11 - 15 \cos^2 \theta)^2 + \sin^2 \phi (1 - 5 \cos^2 \theta)^2 \\ R_2 &= 10 \sin^2 \theta \cos^2 \phi (1 - 3 \cos^2 \theta)^2 + 40 \sin^2 \theta \cos^2 \theta \sin^2 \phi \\ R_3 &= 15 \sin^4 \theta (\cos^2 \theta \cos^2 \phi + \sin^2 \phi) \end{aligned} \quad (4.2)$$

being the components of $R_{|m_J - m'_J|}$: R_0 is the relative amplitude of the $|\Delta m| = 0$ transition, and R_1 , R_2 , and R_3 correspond to $|\Delta m| = 1$, $|\Delta m| = 2$, and $|\Delta m| = 3$ transitions, respectively. The bracket behind the relative amplitude is the Wigner-3j symbol. The relative amplitudes of the $R_{|m_J - m'_J|}$ components are calculated relative

4. Octupole transition of a single $^{172}\text{Yb}^+$ ion

Figure 4.1: Coordinate system for the octupole selection rules. The magnetic field \mathbf{B} is in the $\hat{\mathbf{z}}$ direction. The wave vector of the laser light \mathbf{k} is in the $\hat{\mathbf{x}}\text{-}\hat{\mathbf{z}}$ plane. The angle between \mathbf{k} and $\hat{\mathbf{z}}$ is θ . The polarization of the laser light \mathbf{e} is tipped out of $\hat{\mathbf{x}}\text{-}\hat{\mathbf{z}}$ plane by ϕ .



to θ and ϕ and are shown in Fig. 4.2 and 4.3.

The Wigner $3j$ -symbol and overall intensities of the components are shown in Table 4.1. Using this table and the orientation of the external magnetic field, the laser light, and the polarization, one can calculate the Rabi frequency Ω via equation

$$\Omega = \sqrt{\frac{3I\lambda_0^3\Delta\nu}{2\hbar c_0\pi}} \sqrt{2J'+1} \begin{pmatrix} J' & J' - J & J \\ m'_J & m_J - m'_J & -m_J \end{pmatrix} \quad (4.3)$$

m'_J	m_J	$(3j)^2$	Intensity
-1/2	1/2	3/56	3/56 R_1
-1/2	-1/2	1/14	1/14 R_0
-3/2	1/2	1/28	1/28 R_2
-3/2	-1/2	5/56	5/56 R_1
-5/2	1/2	1/56	1/56 R_3
-5/2	-1/2	3/28	3/28 R_2
-7/2	-1/2	1/8	1/8 R_3

Table 4.1.: Wigner $3j$ -symbol for $J' = 7/2$ and $J = 1/2$ and the corresponding resulted line strengths. m'_J and m_J are the final state and initial state, respectively. The $(3j)^2$ is the square of the Wigner $3j$ -symbol and "Intensity" is the fraction of the intensity of the laser light that is used to drive the corresponding transition.

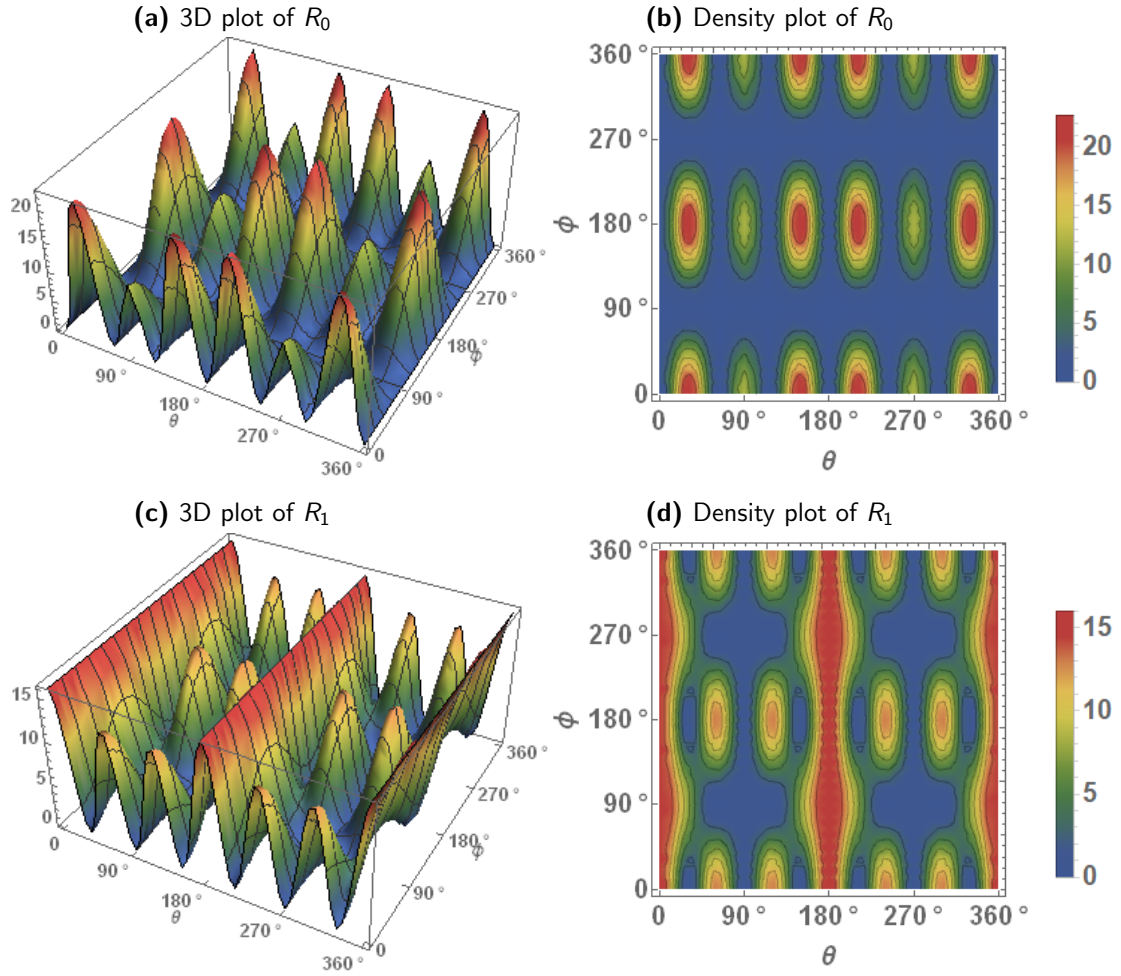


Figure 4.2.: The relative amplitude of R_0 and R_1 relative to θ and ϕ . (a)(b) 3D plot and density plot of the relative amplitude of R_0 . (c)(d) 3D plot and density plot of the relative amplitude of R_1 .

4. Octupole transition of a single $^{172}\text{Yb}^+$ ion

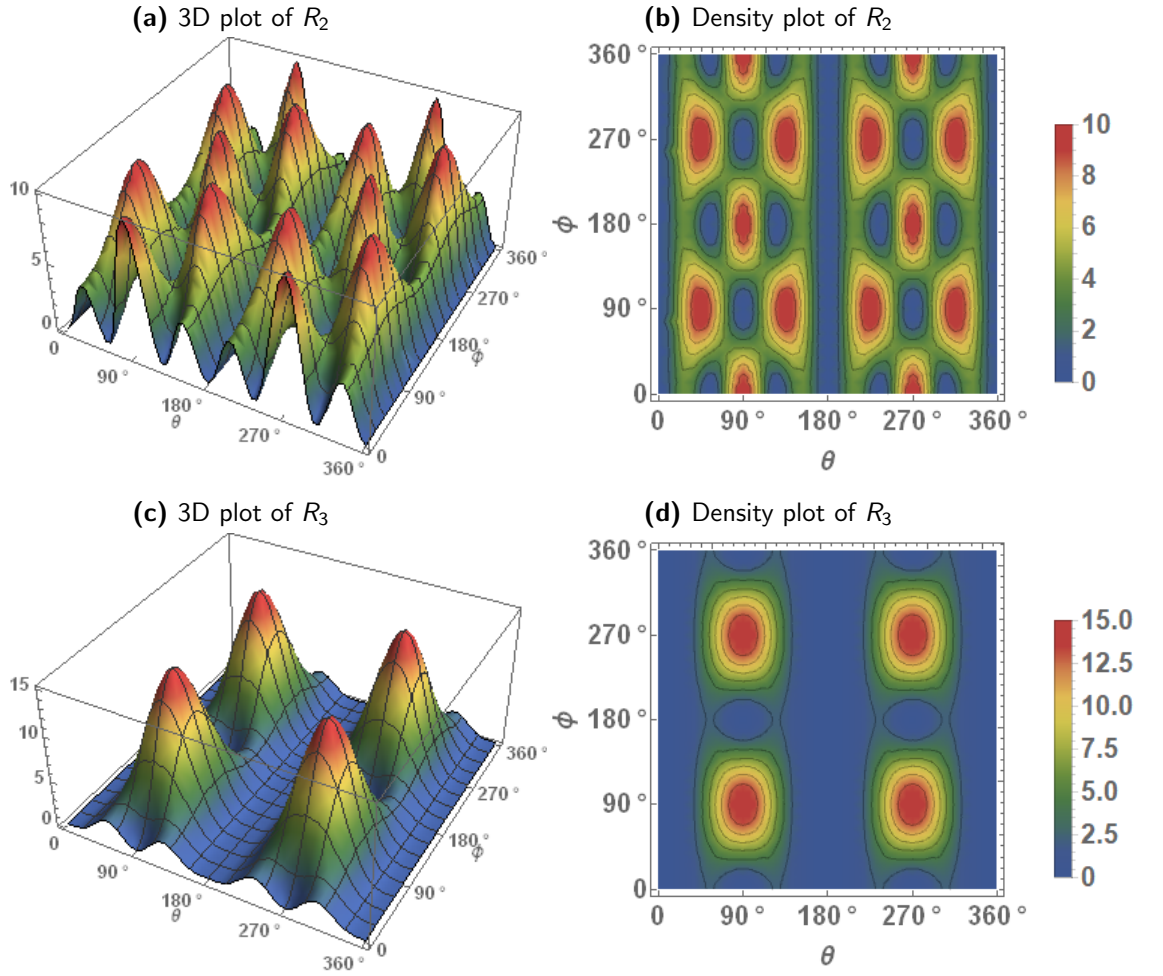


Figure 4.3.: The relative amplitude of R_2 and R_3 relative to θ and ϕ . (a)(b) 3D plot and density plot of the relative amplitude of R_2 . (c)(d) 3D plot and density plot of the relative amplitude of R_3 .

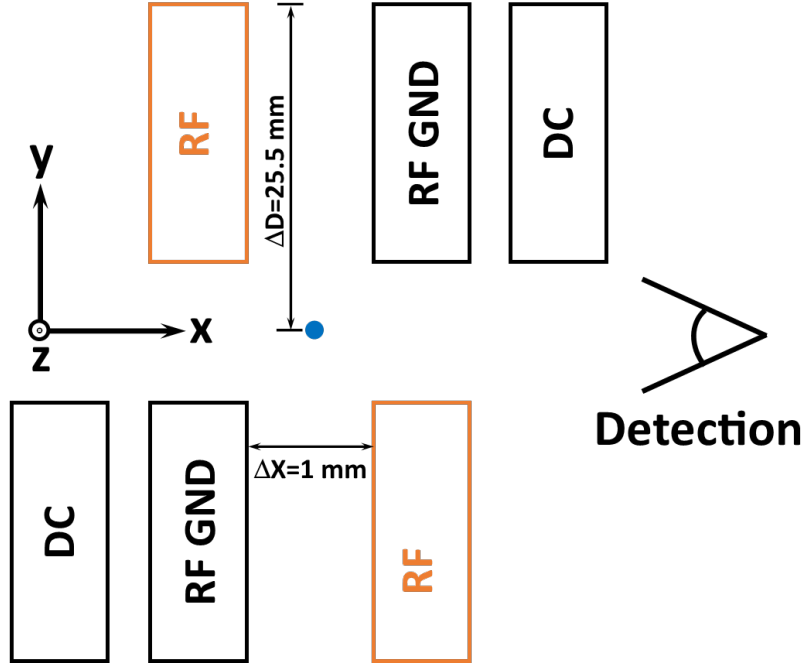


Figure 4.4.: The geometry of the chip trap in the current setup. The 467 nm laser light interrogates the ion at the center of the trap from the \hat{y} -axis. The distance from the ion to the upper edge of the trap is $\Delta D = 25.5$ mm and the distance between the trap electrodes is $\Delta X = 1$ mm. This results in a maximum possible divergence of the beam to be $\tan \alpha = \lambda/(\pi w) = \Delta X/(2\Delta D) = 0.0196$, where λ is the wavelength of the laser and w is the waist radius at the position of the ion. Empirically, the aperture of the upper trap edges should be ≈ 3 times the waist of the laser when it is at the upper edge in order to avoid stray light, i.e. $\tan \alpha' = \tan \alpha/3$.

4.2. Experimental parameters

4.2.1. Beam waist and pulse time

At the position of the ion, we have ≈ 12 mW of power at 467 nm laser light. Due to the chip trap geometry of the current setup shown in Fig. 4.4, the minimum waist at the ion is limited to $22.75 \mu\text{m}$ in order to not hit the edge of the trap and causing stray light with the laser beam. The lenses selected have focal lengths of -50 mm and $+100$ mm with a relative distance of 109 mm as shown in Fig. 3.11. In the setup, the distance between the last lens (the lens with a focal length of $+100$ mm) and the location of the ion is 560 mm. The measured waist after the lens telescope is shown in Fig. 4.5, where the horizontal and vertical waist are $w_h = 38 \mu\text{m}$ and $w_v = 24 \mu\text{m}$, respectively.

4. Octupole transition of a single $^{172}\text{Yb}^+$ ion

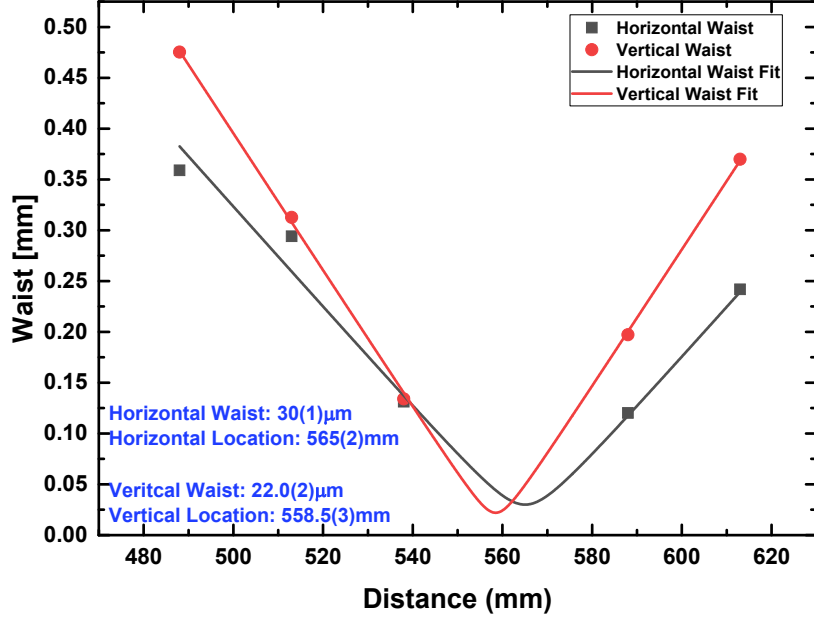


Figure 4.5.: Waist measurement of the 467 nm laser beam after the lens telescope. 560 mm is the position of the ion. The horizontal and vertical waist at the ion are $w_h = 38 \mu\text{m}$ and $w_v = 24 \mu\text{m}$.

The transition we want to interrogate is the $|S, -1/2\rangle \leftrightarrow |F, -1/2\rangle$ transition which has the smallest Zeeman sensitivity of 0.56 MHz/G. With the measured beam waist, the expected time for a π -pulse on the octupole transition is ≈ 54 ms. See Appendix A.1 for calculation details.

4.2.2. Beam alignment procedure

We want to interrogate the $|S, -1/2\rangle \leftrightarrow |F, -1/2\rangle$ transition with a Zeeman sensitivity of 0.56 MHz/G. It is a $|\Delta m| = 0$ transition. For maximum coupling strength, the parameter R_0 in Eq. 4.2 needs to be maximized. The geometry of our setup is shown in Fig. 4.6. The 467 nm laser beam will propagate along the \hat{y} -axis and is anti-parallel to the 411 nm quadrupole laser. The magnetic field points along the H2 direction. So the angle between the magnetic field and the wave vector of the laser beam is fixed at $\theta = 90^\circ$. Therefore, R_0 is at maximum when the polarization of the laser is parallel

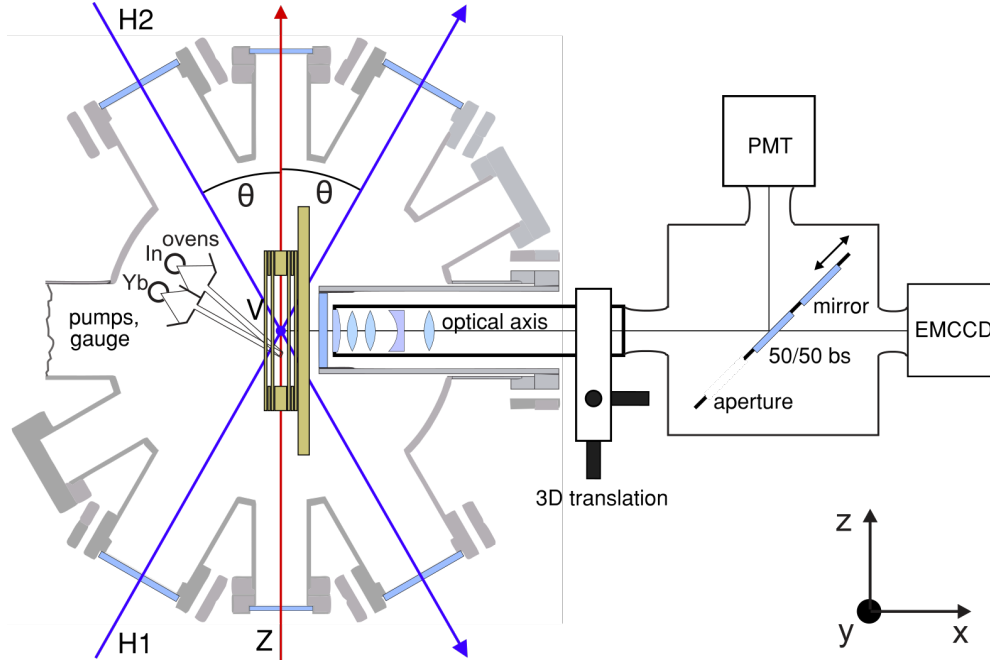


Figure 4.6.: Geometry of the experimental chamber taken from [40]. The magnetic field for the Zeeman splitting points along the H2 direction.

($\phi = 0$) or anti-parallel ($\phi = 180^\circ$) to the direction of the magnetic field as shown in Fig. 4.7.

In order to have the laser beam aligned properly, the quadrupole transition of the $^{172}\text{Yb}^+$ is interrogated while alignment of the 467 nm laser beam is done. To obtain the optimal alignment of the 467 nm laser beam, the induced AC-Stark shift on the quadrupole carrier frequency is monitored. When the alignment is optimal, the induced AC-Stark shift is at its maximum.

The interrogation of the quadrupole transition involves several lasers, which will be briefly described with the relevant level scheme of $^{172}\text{Yb}^+$, as shown in Fig. 4.8. The 370 nm laser is used in the process of Doppler cooling, optical pumping, and state detection. Additional cooling can be done by implementing sideband cooling with the 411 nm and 1650 nm laser. The branching ratio is 0.83 [?]. Due to the population of metastable states during the cooling process, we have the repumpers 639 nm and 935 nm that close the cooling cycles. The 467 nm octupole transition is used for the test of a possible LV and has a lifetime of ≈ 6 years [33].

4. Octupole transition of a single $^{172}\text{Yb}^+$ ion

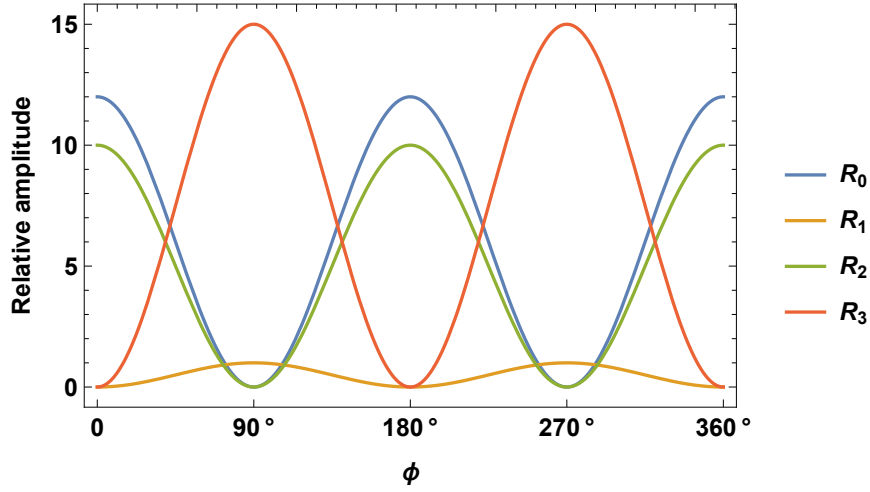


Figure 4.7.: The amplitude of the $R_{|m_J-m'_J|}$ components relative to ϕ . The blue, yellow, green, and orange lines are R_0 to R_3 , respectively. The current setup sets the angle between the magnetic field and the wave vector of the laser beam to be fixed at $\theta = 90^\circ$. The transition to be interrogated is $|S, -1/2\rangle$ to $|F, -1/2\rangle$. The transition is chosen because it has the smallest Zeeman sensitivity of 0.56 MHz/G. The maximum relative amplitude of R_0 is achieved when the polarization of the laser is parallel ($\phi = 0$) or anti-parallel ($\phi = 180^\circ$) to the direction of the magnetic field.

The quadrupole transition we interrogate is the $|S, -1/2\rangle \leftrightarrow |D, -5/2\rangle$ transition. The experimental pulse sequence is shown in Fig. 4.9. With a trapped $^{172}\text{Yb}^+$ ion, a reference image is first taken to determine whether the ion is initially in the ground state. Cycles with dark reference images are discarded. After the ion is being Doppler cooled, it ion is optically pumped with a σ^- circular polarized 370 nm laser beam to the $|S, -1/2\rangle$. In the spectroscopy section, the frequency of a double-pass AOM which has a center frequency of 200 MHz can be varied to tune the laser frequency on resonance with the carrier frequency of the quadrupole transition. The sequence is followed by detection of the population of the ion at the excited state and then repumping it back to the ground state.

In Fig. 4.10, the quadrupole carrier transition frequency with the 467 nm laser being turned on or off is measured. Each measurement point is the average of 100 pulse sequence cycles. As the frequency of the 411 nm quadrupole laser is scanned with a double-pass AOM, with the frequency gap between the two peaks in the figure being 850 Hz, a maximum AC-Stark shift of 1.7 kHz is obtained

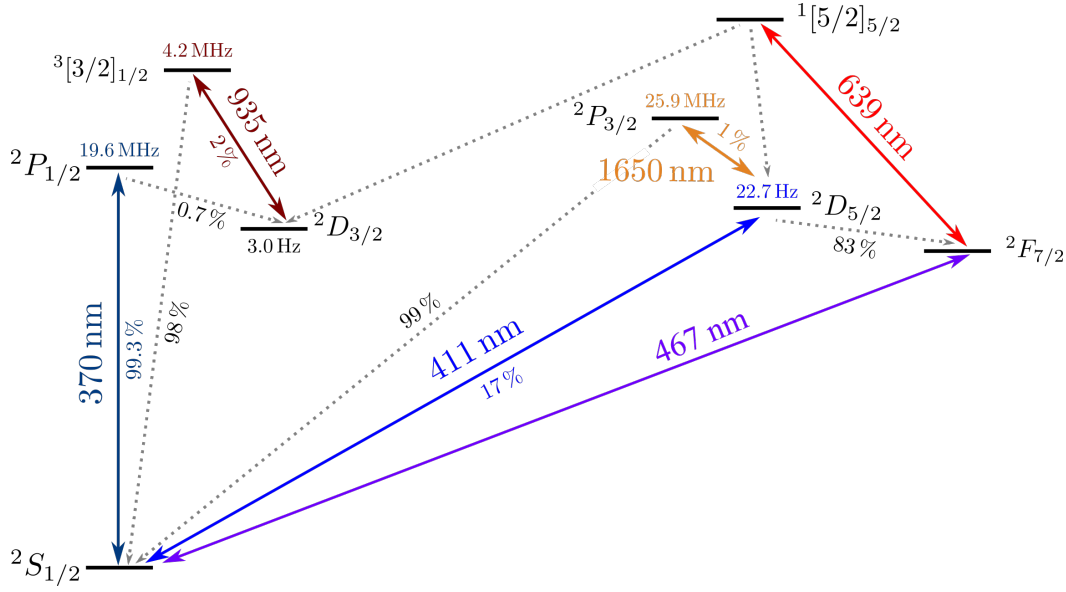


Figure 4.8.: Reduced level scheme of $^{172}\text{Yb}^+$ from [41]. The 370 nm laser is used in the process of Doppler cooling, optical pumping, and state detection. Additional cooling can be done by implementing sideband cooling with the 411 nm and 1650 nm laser. Due to the population of metastable states during the cooling process, we have the repumpers 639 nm and 935 nm that close the cooling cycles. The 467 nm octupole transition is used for the test of a possible LV.

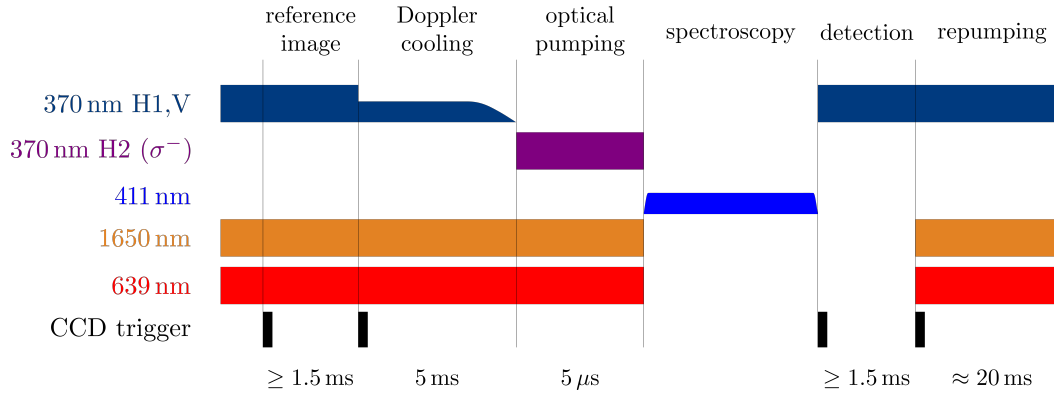


Figure 4.9.: The 411 nm quadrupole spectroscopy sequence. The 935 nm repumping laser is always on, therefore it is not shown in the pulse sequence.

4. Octupole transition of a single $^{172}\text{Yb}^+$ ion

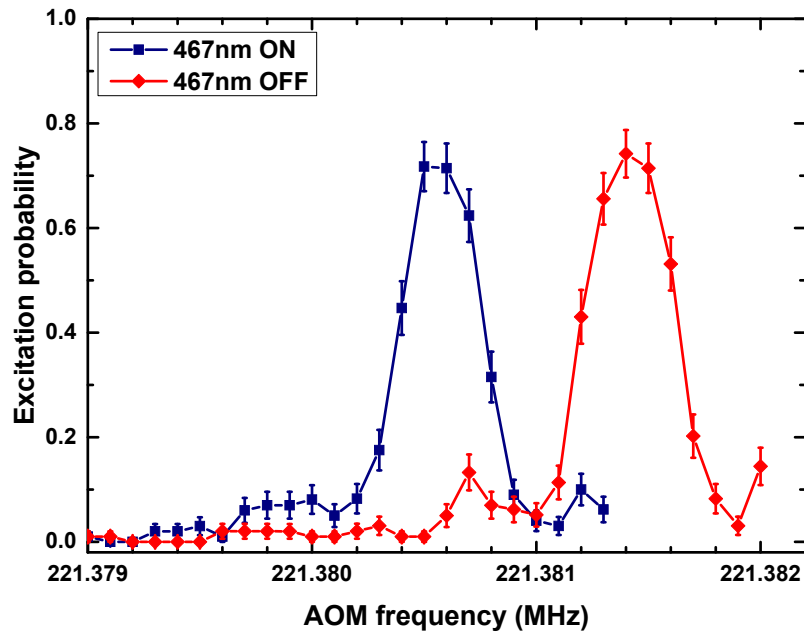


Figure 4.10.: AC Stark shift of the quadrupole transition due to 467nm octupole laser. The red and blue line correspond to the 467nm octupole laser being off and on. The frequency gap between the two peaks is ≈ 850 Hz. But since a double-pass AOM is implemented to vary the frequency of the laser, the AC-Stark shift is 1.7 kHz.

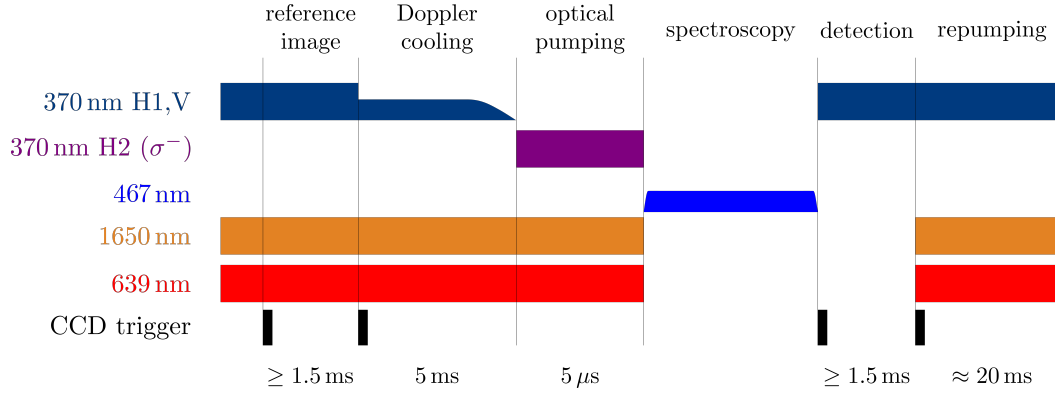


Figure 4.11.: The 467 nm octupole spectroscopy sequence. The 935 nm repumper laser is not shown because it is always on during the pulse sequence.

4.2.3. Pulse sequence

To interrogate the octupole transition, a similar pulse sequence is used as for the quadrupole transition. Here, the laser frequency is steered by means of a double-pass AOM with a center frequency of 110 MHz as shown in Fig. 3.11. The frequency difference between the two Yb^+ isotopes are shown in Fig. 3.1 to be 4711.5 MHz with an uncertainty of 700 kHz. With the HF AOM that provides 2320.1 MHz of frequency shift on the 934 nm and the 200 MHz of frequency shift provided by the AOM on the 467 nm breadboard, the frequency difference is reduced to 223.6 MHz with an uncertainty of 700 kHz. With the double-pass AOM, the frequency at the AOM is half of the value, being 111.4 MHz. To find the transition, we steer the frequency of the laser with a range of ± 500 kHz with respect to 111.4 MHz on the double-pass AOM. The sequence is presented in Fig. 4.11.

5. Summary and outlook

This thesis contributes toward the realization of the experiment to test LV with multiple $^{172}\text{Yb}^+$ ions. We first discussed four different schemes of detecting a possible LV signal. With the comparison of their sensitivities and the effect of magnetic field noise to each scheme, we conclude with following the approach of scheme 4 which implements dynamical decoupling on the $^2F_{7/2}$ manifold. With a chosen ion number of 10, an interrogation time of 10 s, and an averaging time of 120 h, the sensitivity of the experiment to the symmetry-breaking $c'_{\mu\nu}$ tensor element is $\Delta C_0^{(2)} = 4.7 \times 10^{-22}$ which would be a factor of 17 better than the current limit [25].

The laser needed for the interrogation of the $^2S_{1/2} \leftrightarrow ^2F_{7/2}$ octupole transition has been set up. The laser power at the position of the ion is 12 mW. With this power and the beam waist at the ion measured as $w_h = 38 \mu\text{m}$ and $w_v = 24 \mu\text{m}$, the corresponding π -pulse time is calculated to be ≈ 54 ms. The alignment of the octupole laser has been done via monitoring the 467 nm laser induced AC-Stark shift on the quadrupole carrier frequency.

The next step of the experiment is to find the resonance frequency of the octupole transition. Therefore, we will make use of the rapid adiabatic passage [42] (RAP) technique. It is a method to flip the atomic spin from the ground state to the excited state while scanning the excitation laser in a certain frequency interval. The condition it needs here are that the detuning of the scan range should be much larger than the Rabi frequency and the detuning varies slow enough but faster with respect to the atomic lifetime. After reducing the range of uncertainty with the RAP, a carrier frequency scan will be done to precisely obtain the resonance frequency of the octupole transition. Having found the resonance frequency, we will implement the magnetic field coil for dynamical decoupling of the $^2F_{7/2}$ manifold.

The longer the optical pulse time, the more likely that magnetic field noise will cause the state of the ion to dephase. Therefore, to prevent the state from dephasing, we need to reduce the pulse time (or increase the Rabi frequency). From Eq. 4.3, we see that the Rabi frequency is proportional to the square root of the intensity. However, due to the limited amount of laser power we have, the intensity of the 467 nm laser cannot be increased further. Another way to reduce the π -pulse time is to increase

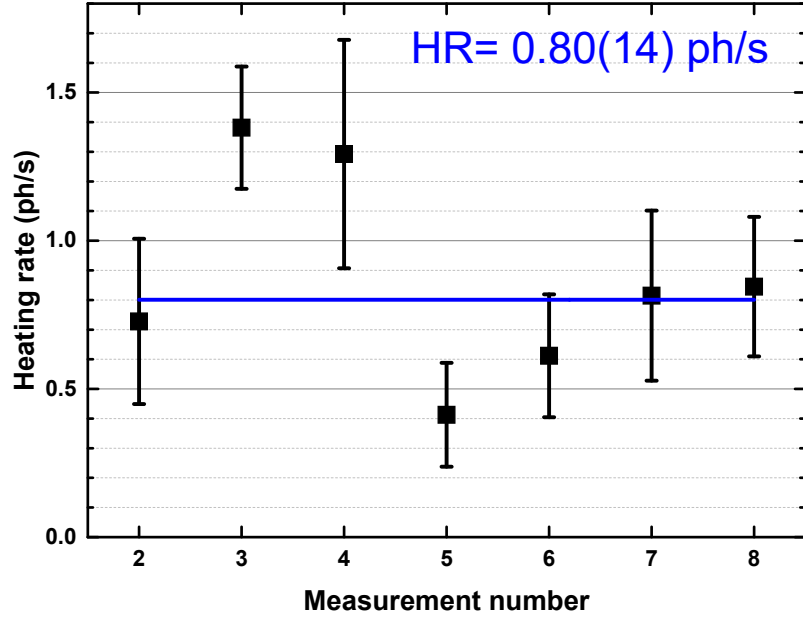


Figure 5.1.: Measurement of the heating rate. The \hat{x} -axis is the measurement number and the \hat{y} -axis is the heating rate in units of phonon/second.

the coupling strength. For example, a huge fraction (60 %) of the intensities of 467 nm laser are being distributed to the $|\Delta m| = 2$ transitions with the current setup. If the angle θ can be set to 30° , then the parameter R_0 is maximized and the π -pulse time is reduced to ≈ 40 ms. If we set $\theta = 0$, then there will only be $|\Delta m| = 1$ transitions. However, the π -pulse time for the $|S, \mp 1/2\rangle \leftrightarrow |F, \pm 1/2\rangle$ ($|\Delta m| = 1$) is still only ≈ 54 ms.

We aim to use 10 ions for the test of LV. After the interrogation of the octupole transition in a single Yb^+ ion, the next step is to select the desired secular frequencies for trapping 10 ions in an ion chain. The radial secular frequency of $\omega_r = 2\pi \times 600$ kHz is chosen. At this frequency, the heating rate of the trap is ≈ 1 phonon/s as shown in Fig. 5.1. With the low heating rate, we can extend the interrogation time of the experiment without a dephasing of the ion states due to heating.

The number of ions trapped in a chain determines the upper limit of the axial

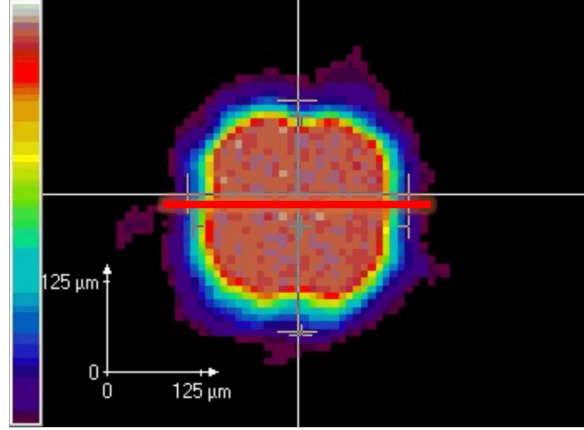


Figure 5.2.: Beam profile of a 411 nm after passing through the phase plate. The red thick bar on the beam profile is the cross-section chosen for the evaluation of the fluctuation of the intensities.

secular frequency. To determine the maximum ω_z , we compare ω_z and ω_r with the given equation [43]

$$\frac{\omega_r}{\omega_z} > 0.73N^{0.86}, \quad (5.1)$$

where N is the maximum number of ions that can be obtained while maintaining a linear ion chain with a given ratio between the radial and axial secular frequency. The maximum ω_z with a radial secular frequency of $\omega_r = 2\pi \times 600$ kHz is $\omega_z \approx 2\pi \times 100$ kHz. With these secular frequencies, the ion chain length is calculated to be $\approx 75 \mu\text{m}$.

The ions in the chain all need to be interrogated with the same Rabi frequency, hence the intensities acting on the ions must be equal. First tests with a phase plate¹ have been carried out. The advantage of a phase plate is that it changes the beam profile of the incident beam from Gaussian into a flattop. An example of the beam profile at 411 nm being flattened is shown in Fig. 5.2.

To see how much the intensities deviate on the flattop, a horizontal cross-section of the image is exported and evaluated. The cross-section taken is the red bar shown in Fig. 5.2. The exported data is shown in Fig. 5.3. The $\hat{\mathbf{x}}$ -axis and $\hat{\mathbf{y}}$ -axis are the location of the measurement points on the camera and the signal counts are proportional to the intensity at the respective pixel of the camera. The pixel size is $10 \mu\text{m}$. From the data, the maximum count is 975 counts, the maximum difference between each

¹TOPAG GTH-3.6-1.75

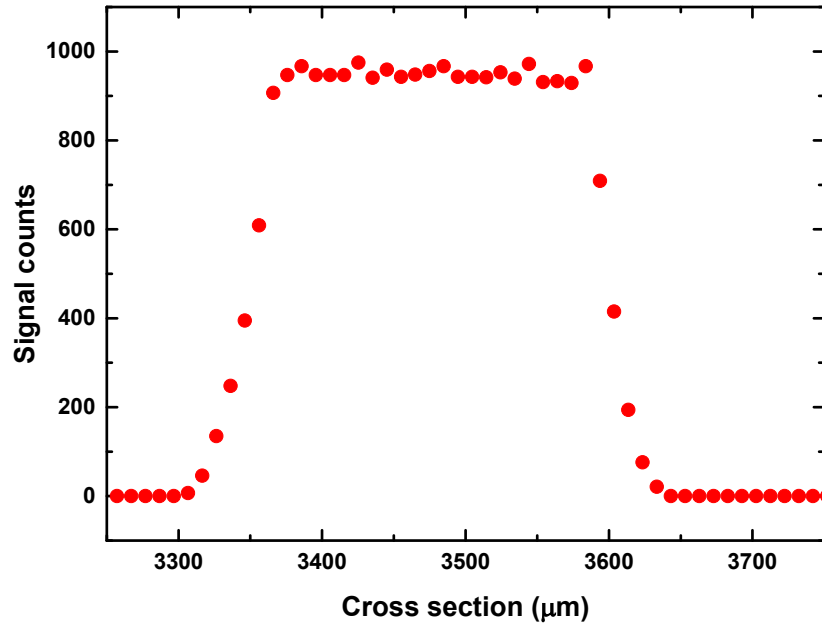


Figure 5.3.: The exported data of the cross-section chosen in Fig. 5.2. The \hat{x} -axis is the location of the measurement points on the camera and the \hat{y} -axis is the signal counts. The distance between each measurement point is $\Delta x = 10 \mu\text{m}$.

measurement points is 68. Therefore, the homogeneity of the phase plate is calculated to be 7 % relative to the maximum intensity.

Since the ion chain length is $\approx 75\,\mu\text{m}$, we choose the flattop to be $90\,\mu\text{m}$ in the axial direction (the ion chain principle axis) and focus the radial axis (vertical to the principle axis) of the flattop to $30\,\mu\text{m}$. With these values, the calculated π -pulse time is $\approx 74\,\text{ms}$ with a Fourier-limited linewidth of $\approx 12\,\text{Hz}$. The fluctuation of the AC-Stark shift is estimated to be $\approx 8\,\text{Hz}$. See Appendix A.2 for calculation details. Assuming that the center ion of the ion chain is interrogated perfectly, a maximum difference in the AC-Stark shift of $8\,\text{Hz}$ on other ions would cause a loss in intensity of more than 50 %. We conclude that this phase plate cannot be used for the LV experiment. If the intensity fluctuation is 4 %, then the fluctuation of the AC-Stark shift is estimated to be $\approx 5\,\text{Hz}$ which would be within the Fourier linewidth. Hence, we need to implement a phase plate with homogeneity of 2 % relative to the average intensity or a spatial light modulator which can be programmed such that the intensity at each ion is the same.

Appendices

A. Mathematica Code

A.1. Calculation of Rabi frequency and π -pulse time

(*Natural constants*)

```
h = 6.626069 * 10-34; (*Planck's Constant in J.s*)  
hbar = h / (2 *  $\pi$ );  
 $\mu$ B = 9.27400899 * 10-24; (*Bohr Magnetron*)  
c0 = 299 792 458; (*Speed of Light in m/s*)
```

(*172Yb LV test parameter*)

```
P467 = 12 * 10-3; (*Power in W*)  
 $\lambda$  = 467 * 10-9; (*wavelength in m*)  
w01 = 38 * 10-6; (*waist radius in m*)  
w02 = 24 * 10-6; (*waist radius in m*)  
Intens = 2 * P467 / ( $\pi$  * w01 * w02);  
lifetime = 1.3 * 108; (*lifetime of Yb octupole state in s*)  
 $\gamma$  = 1 / (2 *  $\pi$  * lifetime); (*Linewidth of the transition in Hz*)
```

(*Current geometry (octupole selection rules): B-field and wave vector is at $\theta=90^\circ$ *)

```
 $\theta$  = 90 °;  
 $\phi$  = 180 °;  
 $R_0$  = 12 (Sin[ $\theta$ ])2 (Cos[ $\phi$ ])2 (1 - 5 (Cos[ $\theta$ ])2)2;  
 $R_1$  = (Cos[ $\theta$ ])2 (Cos[ $\phi$ ])2 (11 - 15 (Cos[ $\theta$ ])2)2 + (Sin[ $\phi$ ])2 (1 - 5 (Cos[ $\theta$ ])2)2;  
 $R_2$  = 10 (Sin[ $\theta$ ])2 (Cos[ $\phi$ ])2 (1 - 3 (Cos[ $\theta$ ])2)2 + 40 (Sin[ $\theta$ ])2 (Cos[ $\theta$ ])2 (Sin[ $\phi$ ])2;  
 $R_3$  = 15 (Sin[ $\theta$ ])4 ((Cos[ $\theta$ ])2 (Cos[ $\phi$ ])2 + (Sin[ $\phi$ ])2);
```

$$\eta = \frac{\frac{1}{14} * R_0}{\frac{3}{28} * R_2 + \frac{1}{28} * R_2 + \frac{1}{14} * R_0};$$

(*Rabi frequency calculation*)

```
v1 = Sqrt[3 * Intens *  $\eta$  * ThreeJSymbol[{7/2, -1/2}, {3, 0}, {1/2, 1/2}]2 *  
   $\lambda^3$  *  $\gamma$  / (2 * hbar * c0 *  $\pi$ )] * Sqrt[2 * 7/2 + 1] / (2 *  $\pi$ );  
(*Rabi frequency from -1/2 to -1/2 in Hz*)  
pitime1 = 1 / (2 * v1);
```

```
Print["R0=", R0]
```

```
Print["R1=", R1]
```

```
Print["R2=", R2]
```

```
Print["R3=", R3]
```

```
Print["Relative percentage of the intensity for -1/2 to -1/2 transition: ",  
  N[ $\eta$ ] * 100, " %"]
```

```
Print["Theoretical Rabi frequency: 2 $\pi$  x ", v1, " Hz"]
```

```
Print["Theoretical  $\pi$ -pulse time: ", 103 * pitime1, " ms"]
```

```
Print["Theoretical Fourier-limited linewidth: ", 0.9 / pitime1, " Hz"]
```

$R_0=12$

$R_1=0$

$R_2=10$

$R_3=0$

Relative percentage of the intensity for $-1/2$ to $-1/2$ transition: 37.5 %

Theoretical Rabi frequency: $2\pi \times 9.25307$ Hz

Theoretical π -pulse time: 54.0361 ms

Theoretical Fourier-limited linewidth: 16.6555 Hz

A.2. Calculation of the AC-Stark shift and relative shift due to intensity fluctuation

(*Natural constants*)

```
h = 6.626069 * 10-34; (*Planck's Constant in J.s*)
hbar = h / (2 *  $\pi$ );
 $\mu$ B = 9.27400899 * 10-24; (*Bohr Magneton*)
c0 = 299 792 458; (*Speed of Light in m/s*)
```

(*Result of 171Yb clock*)

```
PREF = 10 * 10-3; (*Power in W*)
w00 = 20 * 10-6; (*Waist at the ion in m*)
IntensRef = 2 * PREF / ( $\pi$  * w002); (*Intensity in W/m2*)
pulsemax = 0.335; (*Coherence time in s*)
pitime = 0.018; (*minimum  $\pi$ -pulse time in s*)
lightshift = 1090; (*AC-Stark shift in Hz*)
 $\nu$  = 1 / (2 * pitime); (*Rabi frequency in Hz*)
ACStark = 0.0000267; (*in Hz / (W/m2) , estimated from Nils' thesis*)
```

```
Print["Rabi frequency of 171Yb octupole:  $2\pi \times$  ",  $\nu$ , " Hz"]
```

(*172Yb LV test parameter*)

```
P467 = 12 * 10-3; (*Power in W*)
 $\lambda$  = 467 * 10-9; (*wavelength in m*)
w01 = 90 * 10-6; (*units in m*)
w02 = 30 * 10-6; (*units in m*)
Intens = P467 / (w01 * w02);
lifetime = 1.3 * 108; (*lifetime of Yb octupole state in s*)
 $\gamma$  = 1 / (2 *  $\pi$  * lifetime); (*Linewidth of the transition in Hz*)
```

(*Current geometry (octupole selection rules): B-field and wave vector is at $\theta=90^\circ$ *)

```
 $\theta$  = 90 °;
 $\phi$  = 180 °;
 $R_0$  = 12 (Sin[ $\theta$ ])2 (Cos[ $\phi$ ])2 (1 - 5 (Cos[ $\theta$ ])2)2;
 $R_1$  = (Cos[ $\theta$ ])2 (Cos[ $\phi$ ])2 (11 - 15 (Cos[ $\theta$ ])2)2 + (Sin[ $\phi$ ])2 (1 - 5 (Cos[ $\theta$ ])2)2;
 $R_2$  = 10 (Sin[ $\theta$ ])2 (Cos[ $\phi$ ])2 (1 - 3 (Cos[ $\theta$ ])2)2 + 40 (Sin[ $\theta$ ])2 (Cos[ $\theta$ ])2 (Sin[ $\phi$ ])2;
 $R_3$  = 15 (Sin[ $\theta$ ])4 ((Cos[ $\theta$ ])2 (Cos[ $\phi$ ])2 + (Sin[ $\phi$ ])2);
```

```
Print["R0=", R0]
Print["R1=", R1]
Print["R2=", R2]
Print["R3=", R3]
```

$$\eta = \frac{\frac{1}{14} * R_0}{\frac{3}{28} * R_2 + \frac{1}{28} * R_2 + \frac{1}{14} * R_0};$$

```
Print["Relative percentage of the intensity for -1/2 to -1/2 transition: ",
N[ $\eta$ ] * 100, " %"]
```

(*Rabi frequency calculation*)

```
 $\nu_1$  = Sqrt[3 * Intens *  $\eta$  * ThreeJSymbol[{7 / 2, -1 / 2}, {3, 0}, {1 / 2, 1 / 2}]2 *
```



```


$$\lambda^3 * \gamma / (2 * \hbar * c_0 * \pi)] * \text{Sqrt}[2 * 7 / 2 + 1] / (2 * \pi);$$

(*Rabi frequency from -1/2 to -1/2 in Hz*)
pitime1 = 1 / (2 * v1);

Print["Theoretical Rabi frequency:  $2\pi \times$  ", v1, " Hz"]
Print["Theoretical  $\pi$ -pulse time: ",  $10^3 * \text{pitime1}$ , " ms"]

relIntensity = 0.07;
resShift = N[Intens * relIntensity * ACStark];

Print["Theoretical Fourier-limited linewidth: ",  $0.9 / \text{pitime1}$ , " Hz"]
Print["Fluctuation of AC-Stark shift: ", resShift,
      " Hz, if laser power fluctuates by ", relIntensity * 100, " %"]

```

Rabi frequency of ^{171}Yb octupole: $2\pi \times 27.7778$ Hz

$R_0=12$

$R_1=0$

$R_2=10$

$R_3=0$

Relative percentage of the intensity for -1/2 to -1/2 transition: 37.5 %

Theoretical Rabi frequency: $2\pi \times 6.74002$ Hz

Theoretical π -pulse time: 74.1837 ms

Theoretical Fourier-limited linewidth: 12.132 Hz

Fluctuation of AC-Stark shift: 8.30667 Hz, if laser power fluctuates by 7. %

Acronyms

LS	Lorentz symmetry
LV	Lorentz violation
SME	Standard Model Extension
UFF	Universality of Free Fall
LPI	Local Position Invariance
LLI	Local Lorentz Invariance
RF	Radio-frequency
HF	High frequency
AOM	Acousto-optic modulator
SHG	Second-harmonic-generation
ECDL	External-cavity diode laser
ULE	Ultra-low-expansion
SDL	Slave diode laser
OSA	Optical spectrum analyzer
PM	Polarization maintaining
PMT	Photomultiplier tube
SNR	Signal-to-noise ratio
ROI	Region of interest

Bibliography

- [1] David Mattingly. Modern tests of lorentz invariance. *Living Reviews in Relativity*, 8(1):5, Sep 2005. 1
- [2] Ch. Eisele, A. Yu. Nevsky, and S. Schiller. Laboratory test of the isotropy of light propagation at the 10^{-17} level. *Phys. Rev. Lett.*, 103:090401, Aug 2009. 1
- [3] S. Herrmann, A. Senger, K. Möhle, M. Nagel, E. V. Kovalchuk, and A. Peters. Rotating optical cavity experiment testing lorentz invariance at the 10^{-17} level. *Phys. Rev. D*, 80:105011, Nov 2009.
- [4] Albert Abraham Michelson and Edward Williams Morley. On the Relative Motion of the Earth and the Luminiferous Ether. *Am. J. Sci.*, 34:333–345, 1887. 1
- [5] Brett Altschul. Testing electron boost invariance with $2s-1s$ hydrogen spectroscopy. *Phys. Rev. D*, 81:041701, Feb 2010. 1
- [6] R. W. P. Drever. A search for anisotropy of inertial mass using a free precession technique. *The Philosophical Magazine: A Journal of Theoretical Experimental and Applied Physics*, 6(65):683–687, 1961.
- [7] M. A. Hohensee, N. Leefer, D. Budker, C. Harabati, V. A. Dzuba, and V. V. Flambaum. Limits on violations of lorentz symmetry and the einstein equivalence principle using radio-frequency spectroscopy of atomic dysprosium. *Phys. Rev. Lett.*, 111:050401, Jul 2013. 1, 6, 7
- [8] V. W. Hughes, H. G. Robinson, and V. Beltran-Lopez. Upper limit for the anisotropy of inertial mass from nuclear resonance experiments. *Phys. Rev. Lett.*, 4:342–344, Apr 1960.
- [9] Arthur Matveev et al. Precision measurement of the hydrogen $1s-2s$ frequency via a 920-km fiber link. *Phys. Rev. Lett.*, 110:230801, Jun 2013.
- [10] M. Smiciklas, J. M. Brown, L. W. Cheuk, S. J. Smullin, and M. V. Romalis. New test of local lorentz invariance using a $^{21}\text{Ne-Rb-K}$ comagnetometer. *Phys. Rev. Lett.*, 107:171604, Oct 2011. 1

- [11] V. Alan Kostelecký and Stuart Samuel. Spontaneous breaking of lorentz symmetry in string theory. *Phys. Rev. D*, 39:683–685, Jan 1989. 1
- [12] John Ellis, N. E. Mavromatos, and D. V. Nanopoulos. Probing models of quantum space-time foam. 1
- [13] Rodolfo Gambini and Jorge Pullin. Nonstandard optics from quantum space-time. *Phys. Rev. D*, 59:124021, May 1999. 1
- [14] Moritz Nagel, Stephen R. Parker, Evgeny V. Kovalchuk, Paul L. Stanwix, John G. Hartnett, Eugene N. Ivanov, Achim Peters, and Michael E. Tobar. Direct terrestrial test of Lorentz symmetry in electrodynamics to 10¹⁸. *Nature Communications*, 6:8174, September 2015. 1
- [15] Peter Wolf, Frédéric Chapelet, Sébastien Bize, and André Clairon. Cold atom clock test of lorentz invariance in the matter sector. *Phys. Rev. Lett.*, 96:060801, Feb 2006. 1
- [16] F. Allmendinger, W. Heil, S. Karpuk, W. Kilian, A. Scharth, U. Schmidt, A. Schnabel, Yu. Sobolev, and K. Tullney. New limit on lorentz-invariance- and *cpt*-violating neutron spin interactions using a free-spin-precession ³He-¹²⁹Xe comagnetometer. *Phys. Rev. Lett.*, 112:110801, Mar 2014. 1
- [17] T. Pruttivarasin, M. Ramm, S. G. Porsev, I. I. Tupitsyn, M. S. Safronova, M. A. Hohensee, and H. Häffner. MichelsonMorley analogue for electrons using trapped ions to test Lorentz symmetry. *Nature*, 517:592, January 2015. 1, 5, 14
- [18] Eli Megidish, Joseph Broz, Nicole Greene, and Hartmut Häffner. Entanglement enhanced precision test of local Lorentz invariance. *arXiv:1809.09807 [quant-ph]*, September 2018. arXiv: 1809.09807. 1, 6, 8
- [19] G. W. Bennett et al. Search for lorentz and *cpt* violation effects in muon spin precession. *Phys. Rev. Lett.*, 100:091602, Mar 2008. 1
- [20] P. Adamson et al. Search for lorentz invariance and *cpt* violation with muon antineutrinos in the minos near detector. *Phys. Rev. D*, 85:031101, Feb 2012. 1
- [21] M. G. Aartsen et al. Neutrino interferometry for high-precision tests of Lorentz symmetry with IceCube. *Nature Physics*, 14(9):961–966, September 2018. 1
- [22] V. Alan Kostelecký and Neil Russell. Data tables for lorentz and *cpt* violation. *Rev. Mod. Phys.*, 83:11–31, Mar 2011. 1
- [23] Don Colladay and V. Alan Kostelecký. CPT violation and the standard model. *Phys. Rev. D*, 55:6760–6774, Jun 1997.

-
- [24] D. Colladay and V. Alan Kostelecký. Lorentz-violating extension of the standard model. *Phys. Rev. D*, 58:116002, Oct 1998. 1, 6
 - [25] Christian Sanner, Nils Huntemann, Richard Lange, Christian Tamm, Ekkehard Peik, Marianna S. Safronova, and Sergey G. Porsev. Optical clock comparison test of Lorentz symmetry. *arXiv:1809.10742 [physics, physics:quant-ph]*, September 2018. arXiv: 1809.10742. 1, 7, 53
 - [26] Christian F Roos. Ion trap quantum gates with amplitude-modulated laser beams. *New Journal of Physics*, 10(1):013002, January 2008. 6, 17
 - [27] Anders Sørensen and Klaus Mølmer. Quantum computation with ions in thermal motion. *Phys. Rev. Lett.*, 82:1971–1974, Mar 1999.
 - [28] Anders Sørensen and Klaus Mølmer. Entanglement and quantum computation with ions in thermal motion. *Phys. Rev. A*, 62:022311, Jul 2000. 6, 17
 - [29] V. Alan Kostelecký and Charles D. Lane. Constraints on lorentz violation from clock-comparison experiments. *Phys. Rev. D*, 60:116010, Nov 1999. 6, 7
 - [30] V Dzuba, Victor Flambaum, M S. Safronova, Sergey Porsev, T Pruttivarasin, M A. Hohensee, and Hartmut Häffner. Strongly enhanced effects of lorentz symmetry violation in entangled yb+ ions. *Nature Physics*, 12, 07 2015. 8, 23
 - [31] Christopher Gerry and Peter Knight. *Introductory Quantum Optics*. Cambridge University Press, 2004. 9
 - [32] M. Chwalla, K. Kim, T. Monz, P. Schindler, M. Riebe, C.F. Roos, and R. Blatt. Precision spectroscopy with two correlated atoms. *Applied Physics B*, 89(4):483–488, Dec 2007. 10
 - [33] Matthew Roberts. *Spectroscopy of a Single Ytterbium Ion*. PhD thesis, University of London, 1996. 11, 27, 28, 47
 - [34] Peter Blythe. *Optical frequency measurement and ground state cooling of single trapped Yb+ ions*. PhD thesis, University of London, 2004. 11
 - [35] R. Shaniv, R. Ozeri, M. S. Safronova, S. G. Porsev, V. A. Dzuba, V. V. Flambaum, and H. Häffner. New methods for testing lorentz invariance with atomic systems. *Phys. Rev. Lett.*, 120:103202, Mar 2018. 19, 21, 22, 23, 24
 - [36] Norman F. Ramsey. A molecular beam resonance method with separated oscillating fields. *Phys. Rev.*, 78:695–699, Jun 1950. 20
 - [37] R. Shaniv. ”private communication”. 24

- [38] Sebastian Häfner, Stephan Falke, Christian Grebing, Stefan Vogt, Thomas Legero, Mikko Merimaa, Christian Lisdat, and Uwe Sterr. 8×10^{-17} fractional laser frequency instability with a long room-temperature cavity. *Opt. Lett.*, 40(9):2112–2115, May 2015. 27
- [39] R. D. Cowan. *The Theory of Atomic Structure and Spectra*. University of California Press, 1981. 41
- [40] Karsten Pyka. *High-precision ion trap for spectroscopy of Coulomb crystals*. PhD thesis, Leibniz Universitt Hannover, 1983. 47
- [41] Jonas Keller. *Spectroscopic characterization of ion motion for optical clock based on Coulomb crystals*. PhD thesis, Leibniz Universitt Hannover, 2016. 49
- [42] Nikolay V Vitanov, Thomas Halfmann, Bruce W Shore, and Klaas Bergmann. Laser-induced population transfer by adiabatic passage techniques. *Annual Review of Physical Chemistry*, 52(1):763–809, 2001. PMID: 11326080. 53
- [43] A. Steane. The ion trap quantum information processor. *Applied Physics B*, 64(6):623–643, Jun 1997. 55